PARTICLE KINETIC SIMULATION OF HIGH ALTITUDE HYPERVELOCITY FLIGHT

Periodic Research Report

Cooperative Agreement NCC2-582

for the period

January 1, 1993 - August 31, 1993

Submitted to

National Aeronautics and Space Administration
Ames Research Center
Moffett Field, California 94035

Dr. George S. Deiwert, Technical Officer

Thermosciences Division
Dr. Jim Arnold, Chief

Prepared by

ELORET INSTITUTE
1178 Maraschino Drive
Sunnyvale, CA 94087
Phone: 408 730-8422 and 415 493-4710
Telefax: 408 730-1441

Dr. K. Heinemann, President and Grant Administrator
Dr. Brian L. Haas, Co-Principal Investigator

12 October, 1993

In this grant period, the focus has been on enhancement and application of the direct simulation Monte Carlo (DSMC) particle method for computing hypersonic flows of re-entry vehicles. Enhancement efforts dealt with modeling gas-gas interactions for thermal non-equilibrium relaxation processes and gas-surface interactions for prediction of vehicle surface temperatures. Both are important for application to problems of engineering interest. The code was employed in a parametric study to improve future applications, and in simulations of aeropass maneuvers in support of the Magellan mission.

Detailed comparisons between continuum models for internal energy relaxation and DSMC models reveals that several discrepancies exist. These include definitions of relaxation parameters and the methodologies for implementing them in DSMC codes. These issues were clarified and all differences were rectified in a paper (Appendix A) submitted to *Physics of Fluids A*, featuring several key figures in the DSMC community as co-authors and B. Haas as first author. This material will be presented at the Fluid Dynamics meeting of the American Physical Society on November 21, 1993.

The aerodynamics of space vehicles in highly rarefied flows are very sensitive to the vehicle surface temperatures. Rather than require prescribed temperature estimates for spacecraft as is typically done in DSMC methods, a new technique was developed which couples the dynamic surface heat transfer characteristics into the DSMC flow simulation code to compute surface temperatures directly. This model, when applied to thin planar bodies such as solar panels, was described in AIAA Paper No. 93-2765 (Appendix B) and was presented at the Thermophysics Conference in July 1993.

The paper has been submitted to the *Journal of Thermophysics and Heat Transfer*.

Application of the DSMC method to problems of practical interest requires a trade off between solution accuracy and computational expense and limitations. A parametric study was performed and reported in AIAA Paper No. 93-2806 (Appendix C) which assessed the accuracy penalties associated with simulations of varying grid resolution and flow domain size. The paper was also presented at the Thermophysics Conference and will be submitted to the journal shortly.

Finally, the DSMC code was employed to assess the pitch, yaw, and roll aerodynamics of the Magellan spacecraft during entry into the Venus atmosphere at off-design attitudes. This work was in support of the Magellan aerobraking maneuver of May 25-Aug. 3, 1993. Furthermore, analysis of the roll characteristics of the configuration with canted solar panels was performed in support of the proposed "Windmill" experiment. Results were reported in AIAA Paper No. 93-3676 (Appendix D) presented at the Atmospheric Flight Mechanics Conference in August 1993, and were submitted to *Journal of Spacecraft and Rockets*.

Appendix A

RATES OF BORGNAKKE-LARSEN THERMAL RELAXATION IN DIRECT SIMULATION MONTE CARLO METHODS

Brian L. Haas[a]
Eloret Institute, Palo Alto, California 94303

David Hash[b]
North Carolina State University, Raleigh, North Carolina 27695

Graeme A. Bird[c]
University of Sydney, Australia

Forrest E. Lumpkin, III[d]
NASA Ames Research Center, Moffett Field, California 94035

H. A. Hassan[e]
North Carolina State University, Raleigh, North Carolina 27695

ABSTRACT

For internal energy relaxation in rarefied gas mixtures, exact relationships are derived between the selection probability P employed in direct simulation Monte Carlo (DSMC) methods and the macroscopic relaxation behavior dictated from Jeans' equation through collision number Z. These expressions apply to the Borgnakke-Larsen model for internal energy exchange mechanics. Simulation results prove that the common assumption $P = 1/Z$, although it can be a fair approximation, is invalid in general since relaxation rates depend upon the intermolecular potential, the number of internal degrees of freedom, and the selection methodology. Differing definitions of collision number Z appearing in the literature are clarified. As proven theoretically, all relaxation curves coalesce to a single curve when plotted against the cumulative number of collisions, regardless of the intermolecular potential. These same relationships apply for variable Z as well. The present work concludes that DSMC kinetics in gas mixtures only match Jeans-Landau-Teller behavior exactly when prohibiting multiple relaxation events during a single collision.

Corresponding Author: Brian L. Haas
Phone: (415) 604-1145
Fax: (415) 604-0350

Pacs Numbers:

02.70.Lq	Monte Carlo and Statistical Methods
34.50.Ez	Rotational and vibrational energy transfer
47.70.Nd	Nonequilibrium gas dynamics

[a] Research Scientist. Mailing Address: NASA Ames Research Ctr. M/S 230-2, Moffett Field, CA 94035
[b] Research Assistant
[c] Professor Emeritus. Current address: G.A.B. Consulting Ltd., Killara, Australia, 2071
[d] Research Scientist
[e] Professor. Dept. of Mechanical and Aerospace Engineering

I. INTRODUCTION

Direct simulation Monte Carlo (DSMC)[1,2] and its variants[3−8] have proven to be reliable tools in computing rarefied flows. These methods employ thousands or millions of discrete computational particles whose motion and interaction simulate gas dynamics. High temperature, rarefied flows are often characterized by thermal nonequilibrium in which various molecular energy modes do not share a common Boltzmann distribution of energies. Simulating these flows, and the corresponding relaxation gas dynamics, requires application of simple phenomenological models which capture the essential macroscopic behavior while retaining computational efficiency in DSMC methods. Several models have appeared in the literature addressing rotational,[9−11] vibrational,[12−15] and chemical[13,16−20] nonequilibrium. A common element within most of these models is application of the Borgnakke-Larsen method[21] in distributing post-collision thermal energy among the energy modes of a pair of colliding particles. This technique assigns internal and translational energies by sampling from the corresponding equilibrium distributions. Of vital concern, however, is the resulting macroscopic rate at which this technique promotes relaxation of the ensemble gas toward equilibrium.

DSMC methods test colliding particles for possible internal energy exchanges or chemical reactions. The collision selection rules employ probabilities which must be defined so as to result in desired macroscopic relaxation rate behavior. This typically involves identifying a macroscopic rate equation which the simulation attempts to match through appropriate definitions of selection probabilities P. These rate equations often contain parameters such as collision numbers Z, characteristic times τ, or rate coefficients which are estimated from experiments or analysis. Ambiguity regarding specific definitions of the targeted macroscopic rates and coefficients has led to confusion in defining appropriate selection probabilities in DSMC methods. This is particularly evident in studies of rotational relaxation for which the Borgnakke-Larsen collision mechanics are widely used and the relaxation rates may be clearly derived.

In studies of vibrational relaxation, Haas[13] developed a relationship between the appropriate DSMC selection probability P and the resulting Landau-Teller macroscopic relaxation behavior. This relationship was later generalized, allowing for rotational relaxation, by Lumpkin *et al.*[22] in the form of a "correction factor" for collision numbers Z. It was observed that the DSMC probabilities P in general cannot be specified by the assumption $P = 1/Z$, which has been employed throughout the DSMC community. Dissimilar applications of the selection probability and incompatible definitions of collision number led to disagreement among DSMC researchers regarding these correction factors.

The present work clarifies the definitions of macroscopic rate parameters employed in rotational relaxation, including differing interpretations of Jeans' equation.[23] It will be shown that relaxing energies, when plotted against the cumulative number of molecular collisions, lead to a single solution regardless of the assumed intermolecular potential. Differing definitions of the rotational collision number Z and collision time τ_c will be clarified. The two most widely used selection methodologies are discussed, and DSMC rotational relaxation probabilities P specific to each methodology will be derived to match the macroscopic rate equations exactly. Prevalent selection methods cannot reproduce Jeans' equation exactly for the case of heteromolecular collisions, nor can they reproduce Jeans and Laundau-Teller[24] rate behavior for simultaneous rotational and vibrational relaxation. Thus, a new selection methodology is introduced that is better suited to the general case of gas mixtures experiencing multimode internal energy relaxation. Finally, considerations regarding variable Z will be addressed.

II. DEFINITIONS OF RELAXATION TIMES AND COLLISION NUMBERS

Most continuum analyses and computational codes employ some form of the Jeans-Laundau-Teller equation[23,24] for study of internal energy relaxation in gases. For rotational relaxation in an single-species adiabatic reservoir, this equation employs the *instantaneous* equilibrium rotational energy $E_r^*(t)$ and a time constant given by the product of the instantaneous collision time τ_c and a characteristic collision number Z as follows:

$$\frac{dE_r}{dt} = \frac{E_r^*(t) - E_r(t)}{\tau_c \, Z}. \tag{1}$$

Here, E_r is the mean rotational energy per molecule in the ensemble, and t represents time. Note that $E_r^*(t)$ varies proportionally with translational temperature T, which will itself vary in time during relaxation. Similarly, τ_c may vary with T, depending upon the intermolecular potential assumed for the gas. Most DSMC methods employ the Variable Hard Sphere (VHS) model of Bird[25] which assumes rigid-sphere collision mechanics but establishes the collision rate in a manner consistent with an inverse-power potential with exponent α. This parameter varies between the limits for Maxwell molecules ($\alpha = 4$) and hard sphere molecules ($\alpha = \infty$). Employing a collision cross-section of the form $\sigma g^{-4/\alpha}$, where g is the relative translational speed of the pair and σ is a constant, DSMC methods lead to an exact definition of collision time given by

$$\tau_c = \frac{1}{n \sqrt{\frac{\pi}{4}} \left(\frac{2kT}{m^*}\right)^{\frac{1}{2}-\frac{2}{\alpha}} \sigma \, \Gamma\left(2 - \frac{2}{\alpha}\right)}. \tag{2}$$

Here m^* is the reduced mass of the pair, n is the number density, and k is Boltzmann's constant. Note that τ_c is independent of T for Maxwell molecules.

An alternative expression for macroscopic relaxation may be expressed in terms of the *final* equilibrium rotational energy $E_r^*(\infty)$ and a new collision number $\tilde{Z}$ as follows:

$$\frac{dE_r}{dt} = \frac{E_r^*(\infty) - E_r(t)}{\tau_c \, \tilde{Z}}. \tag{3}$$

In order to relate Z and $\tilde{Z}$, it is noted that at any time t for a single species adiabatic reservoir, the first law of thermodynamics yields

$$E_t(t) + E_r(t) = E_o \tag{4}$$

where E_t is the mean translational energy and E_o is the mean total energy which is constant. Moreover, the instantaneous equilibrium mean rotational energy is related to E_t by definition of the thermal DOF for rotation ζ_r (=2 for diatomic species) and translation $\zeta_t = 3$ as follows,

$$E_r^*(t) = \frac{\zeta_r}{\zeta_t} E_t(t). \tag{5}$$

By virtue of Eqs. (4) and (5), the final equilibrium rotational energy is expressed by

$$E_r^*(\infty) = \frac{\zeta_r}{\zeta_t + \zeta_r} E_o \tag{6}$$

which leads to the relation

$$E_r^*(t) - E_r(t) = \left(\frac{\zeta_t}{\zeta_r} + 1\right)\left[E_r^*(\infty) - E_r(t)\right]. \tag{7}$$

Comparing Eqs. (1), (3), and (7), one finds

$$\tilde{Z} = \left(\frac{\zeta_t}{\zeta_t + \zeta_r}\right) Z. \tag{8}$$

Both relaxation equations may be integrated exactly for Maxwell molecules, assuming contant collision numbers and densities in the adiabatic reservoir, leading to the following solutions

$$1 - \frac{E_r(t)}{E_r^*(\infty)} = \exp\left(-\frac{t}{\tau_c\, Z}\,\frac{\zeta_t + \zeta_r}{\zeta_t}\right) = \exp\left(-\frac{t}{\tau_c\, \tilde{Z}}\right). \tag{9}$$

For all other types of molecular interaction, where τ_c is dependent upon temperature, numerical integration is required. Note that the relation expressed in Eq. (8) holds irrespective of the interaction potential; *i.e.*, it is not limited to the case of Maxwell molecules.

As shown in Fig. 1a for particular values of α, both rate equations lead to the same relaxation behavior in the adiabatic reservoir when the collision numbers are related as suggested in Eq. (9). Furthermore, these solutions coalesce to a single relaxation curve in Fig. 1b, regardless of VHS parameter α, when plotted against a time scale $\tilde{t}$ representing the cumulative number of collisions per molecule given analytically by the expression,

$$\tilde{t} \equiv \int_{t=0}^{t} \frac{dt}{\tau_c}. \tag{10}$$

Note that the curve is purely exponential in $\tilde{t}$, relaxing to $1/e$ at $\tilde{t}/\tilde{Z} = 1$.

The conclusion here is that Eqs. (1) and (3) reflect the same relaxation behavior but simply employ differing definitions of the collision number as noted in Eq. (8).

A. Definitions of mean collision time

Since collision numbers are often estimated from observed or computed relaxation behavior, one must ensure that consistent definitions of mean collision time τ_c are employed to reduce the Z data.[26] Many experimental definitions[27] of collision time τ_c are quoted assuming either the Chapman-Enskog (C-E) first approximation for viscosity, or the analogous result derived from simple kinetic theory (KT), leading to the respective expressions,

$$\tau_c\big|_{\text{C-E}} = \frac{16/5\mu}{4P}, \qquad \tau_c\big|_{\text{KT}} = \frac{\pi\mu}{4P}, \tag{11}$$

where $P = nkT$ is pressure and μ is viscosity estimated from experiments. Recall, however, that τ_c is defined by the ratio $\lambda/\langle c\rangle$, where λ is the mean free path and $\langle c\rangle = (8kT/\pi m)^{1/2}$ is the mean thermal speed for molecular mass m. Since λ has unambiguous meaning for VHS molecules regardless of α used in the DSMC technique, Bird[28] determined a clear relationship between λ and μ by employing the Chapman-Enskog first approximation, leading to:

$$\tau_c\big|_{\text{VHS}} = \frac{\left(6 - \frac{4}{\alpha}\right)\left(4 - \frac{4}{\alpha}\right)}{30}\frac{\mu}{P}. \tag{12}$$

One may choose to employ higher-order expressions for viscosity,[29] although the first-order approximation is accurate to within a few percent. More importantly, however, the differences between the τ_c expressions in Eq. (11) and $\tau_c|_{\text{VHS}}$ in Eq. (12) may reach sixty percent for Maxwell molecules because of differing definitions of λ for each theory. The point of this discussion is that one must be careful to understand and apply consistent definitions of Z and τ_c when encountering these rate parameters in experiments, analyses, or computations.

III. RELAXATION PROBABILITIES FOR THE DSMC METHOD

The objective now is to determine the probability P needed in the DSMC method which will yield the macroscopic relaxation behavior identified above. Previous researchers have assumed the simple relation $P = 1/Z$, which is invalid in general. Original efforts to map DSMC probabilities to vibrational relaxation rate parameters by Haas[13] yielded a correction factor which was later generalized and applied to rotation by Lumpkin *et al.*[22] In general, the functional relationship between P and Z depends upon the VHS potential α and the manner in which the probability is applied.

A. Prevalent DSMC selection methods

In the DSMC collision routines, once colliding pairs of particles have been identified, P may be applied for acceptance-rejection to each particle individually regardless of the acceptance-rejection outcome of its partner (called *particle-selection*), or to each pair of particles collectively (called *pair-selection*). The latter method was used by Lumpkin *et al.*, and it relaxes both particles in the pair or neither depending upon the acceptance-rejection outcome. These two methodologies, pair-selection and particle-selection, are used widely in the DSMC community. Intuition may dictate that the probabilities used in the pair-selection method must be equal to one-half of those used by the particle-selection method, however the following discussion will demonstrate that such a simple relationship does not hold.

The relative translational energy E_T of colliding particles near equilibrium is distributed with $\zeta_T = 4 - 4/\alpha$ DOF as a result of biasing due to collision selection.[8] This may differ from $\zeta_t = 3$ DOF associated with the translational energy E_t of an equilibrium ensemble of particles in a reservoir. Biasing due to collision selection plays a significant role in the relaxation of the energy in the reservoir. This becomes apparent in the derivation of the relaxation probabilities for the different selection methodologies. In the original paper of Lumpkin *et al.*, a relation between the relaxation probability and the collision number was defined for the pair-selection method as follows,

$$P_{\text{PAIR}} = \left(\frac{\zeta_T + \zeta_{r_A} + \zeta_{r_B}}{\zeta_T}\right)\frac{1}{Z}, \tag{13}$$

where subscripts A and B pertain to each species in the colliding pair.

From similar arguments, a relationship has been derived for the particle-selection method for a single-species gas,

$$P_{\text{PART}} = \left(\frac{\zeta_T + 2\zeta_r}{2\zeta_r}\right)\left[1 - \sqrt{1 - \left(\frac{\zeta_r}{\zeta_T}\right)\left(\frac{\zeta_T + \zeta_r}{\zeta_T + 2\zeta_r}\right)\frac{4}{Z}}\right]. \tag{14}$$

Using Eq. (14), the ratio of P_{PART} to $1/\tilde{Z}$ is plotted in Fig. 2 for several VHS parameters α. For each curve, note that although the assumption $P = 1/\tilde{Z}$ is valid at a particular value of $\tilde{Z}$, it is invalid in

general. As a result of the quadratic term in Eq. (14), there exists a minimum allowable value of Z to insure that P_{PART} is a real number less than or equal to unity,

$$Z > \begin{cases} 2, & \text{for diatomic hard spheres;} \\ 7/3, & \text{for diatomic Maxwell molecules.} \end{cases}$$

To evaluate the models presented here, adiabatic reservoirs composed of a single diatomic species were simulated during rotational relaxation for VHS parameters $\alpha = \{4, \infty\}$. Each reservoir was initialized with all energy in the translational mode only; *i.e.*, $E_r(0) = 0$. Both selection methodologies were used with a targeted relaxation rate corresponding to $\tilde{Z} = 10$. As plotted in Figs. 3a and 4a, results for simulations employing the assumption $P = 1/\tilde{Z}$ differ from the theoretical curve of Eq. (9) and from one another for particle-selection and pair-selection methodologies, respectively. These differences not only prove the assumption is faulty, but they also demonstrate the dependence of the relaxation rate upon VHS parameter α. Repeating these simulations, using the probability computed from Eqs. (14) and (13), led to the plots in Figs. 3b and 4b which all collapse upon the theoretical curve correctly. The two figures appearing in Ref. (22) demonstrated similar results. Unfortunately, due to a typographical error, the figure legend and caption from each graph were switched with those of the other.

While the pair-selection method enjoys simplicity and computational efficiency, it is not well suited to general gas mixtures involving differing relaxation rates and internal DOF per species. These same difficulties apply for the particle-selection method unless one prohibits the possiblility of both particles relaxing internally during a single binary collision (double relaxation). To explain this problem, note that for rotational relaxation of species A due to collisions with molecules of species B, Jeans' equation is expressed as

$$\left.\frac{dE_{r_A}}{dt}\right|_B = \frac{E^*_{r_A}(t) - E_{r_A}(t)}{\tau_{c_{A|B}}\, Z_{A|B}}. \tag{15}$$

Notice that this expression is independent of the rotational energy E_{r_B} of the partner species. However, for the pair-selection method in the case of heteromolecular collisions, relaxation of A molecules would be influenced by the rotational energy of B molecules since both relax simultaneously. This is also true for the particle-selection method because a possibility exists that both particles will relax during one collision. As a consequence, E_{r_B} would appear in the resulting relaxation rate equations for species A such that it cannot be cast in the form given in Eq. (15) for heteromolecular collisions.

A similar problem arises when coupling rotational and vibrational relaxation. If collisions permit simultaneous relaxation of each mode, the corresponding rate equations for each cannot be cast into the Jeans-Landau-Teller form exactly because vibrational energies would appear in the rotational relaxation rate equation and vice-versa. As derived at the end of the Appendix, however, decoupling the relaxation of each mode does lead to relaxation behavior dictated in the Jeans-Landau-Teller form.

Nonetheless, the methods above work very well for vibrationally-frozen gases in which the rotational energies of colliding species have the same number of DOF and relax at the same rate. Such assumptions are employed frequently in continuum and DSMC computations for real gas flows, although the present work is not limited to these assumptions.

B. General DSMC selection method

The intent of the following is to introduce a new selection methodology which is not restricted to the assumptions above and is therefore applicable to gas mixtures. The method is adapted from the particle-selection method in that probabilities P are applied to each molecule individually within the colliding pair, but the event in which both particles relax is prohibited (called *particle-selection without double relaxation*). This insures that relaxation of A molecules is independent of the energy of B molecules, and the Borgnakke-Larsen mechanics can therefore reproduce the relaxation rate behavior defined in Eq. (15). The appropriate functional form for the relaxation probability P'_{PART} is derived in the Appendix for particle-selection prohibiting double-relaxation in the case of binary collisions in general gas mixtures. When applied to a single-species gas, this relationship is given by

$$P'_{\text{PART}} = 1 - \sqrt{1 - \left(\frac{\zeta_T + \zeta_r}{\zeta_T}\right)\frac{2}{Z}}, \tag{16}$$

where Z was defined in Eq. (1) and is related to $\tilde{Z}$ in Eq. (8). Note that P'_{PART} depends upon the VHS parameter as well as the number of internal DOF experiencing relaxation. Again, restrictions on allowable values Z are imposed by the quadratic term;

$$Z > \begin{cases} 3, & \text{for diatomic hard spheres;} \\ 10/3, & \text{for diatomic Maxwell molecules.} \end{cases}$$

As before, the method is evaluated through the use of an adiabatic reservoir of a single-species diatomic gas. Figure 5 shows relaxation behavior with application of uncorrected and corrected probabilities with the targeted relaxation collision number $\tilde{Z} = 10$. Note that the assumption $P = 1/\tilde{Z}$ is close but not exact. Nonetheless, specific relationships between Z and P may be derived to yield the correct relaxation rate behavior in a single species gas regardless of the selection methodology employed in the DSMC technique. The appropriate function, however, is unique for each particular selection methodology as demonstrated by the differences between Eqs. (13), (14), and (16). Depending upon the methodology employed, however, the approximation $P = 1/\tilde{Z}$ may be fairly accurate under practical flow conditions.

C. Variable relaxation probabilities

Although the results noted above correspond to invariant relaxation rates Z, the expressions for P are not restricted to that assumption. Parker[30] expressed the dependence of Z upon temperature T in a homonuclear diatomic gas. Similar observations were made analytically by Lordi and Mates[31] and experimentally by Carnevale *et al.*[27] For DSMC methods, Parker's expression may be used to evaluate a single value of Z for all collisions within a computational cell of local translational temperature T. It can, however, be computationally expensive to calculate T which may itself be ill-defined in nonequilibrium flows.

Alternatively, Boyd[9] developed an expression for Z which is dependent upon the relative translational energy of individual collisions and which reproduces Parker's expression when integrated over all collisions at equilibrium. However, application of probabilities computed in this manner lead to energy distributions that are biased away from the Boltzmann form assumed in the Borgnakke-Larsen model for relaxation mechanics. As such, the model will fail to achieve detailed balance. Boyd countered this by applying a single "averaged" probability throughout the cell. Abe[10] achieved detailed balance while retaining individual collision-specific probabilities by incorporating the biased distributions in his adaption of the Borgnakke-Larsen model for

relaxation mechanics. Alternatively, one could employ Z as a function of the sum of translational and rotational energies since this would not bias the distributions normally employed in the Borgnakke-Larsen technique to partition the energy into individual modes. The important point is that regardless of the formulation used to determine Z, its relationship to P still applies as defined in the present work.

V. CONCLUDING REMARKS

Distinct relationships exist between the microscopic probabilities P employed at the collision level in DSMC methods and the resulting macroscopic relaxation rate behavior in the gas as described by collision numbers Z. These relationships are sensitive to the selection methodology; *i.e.*, the particular manner in which the probabilities are applied. For relaxation of internal modes through application of the Borgnakke-Larsen model of energy-exchange mechanics, the selection probability is not given generally by the simple assumption $P = 1/Z$. Indeed, it is dependent upon the intermolecular VHS potential and the number of DOF contributing to the relaxation process. Furthermore, there are differing definitions appearing in the literature regarding collision numbers Z and collision times τ_c. In most cases a simple relationship resolves these differing definitions as identified in the present work. It was also observed that regardless of the VHS potential employed, all theoretical relaxation curves coalesce to a single curve when plotted against a time axis representing the cumulative number of molecular collisions. Simulations proved that the DSMC technique leads to the same relaxation behavior as dictated by the macroscopic rate equation only when employing the probabilities derived in the present work, although $P = 1/\tilde{Z}$ can be a fair approximation in practical scenarios when employing the particle-selection methodology. Finally, DSMC kinetics in gas mixtures only match Jeans-Landau-Teller behavior exactly when prohibiting multiple relaxation events during a single collision.

ACKNOWLEDGMENTS

This work is supported in part (for BLH) by NASA Grant NCC2-582, and (for DBH) by a National Science Foundation Fellowship, NASA's Cooperative Agreement NCCI-112, and the Mars Mission Research Center funded by NASA Grant NAGW-1331.

APPENDIX: DERIVATION OF RELAXATION PROBABILITY

The relationship between DSMC probabilities and macroscopic collision numbers can be derived by assessing the effect of relaxation collisions upon the internal energy of the entire ensemble of particles, as a result of Borgnakke-Larsen mechanics, and casting the resulting expression into the form dictated in Eq. (1). The following development applies to the particle-selection methodology without double-relaxation, a technique most readily extended for general gas mixtures. The derivation for particle-selection including double-relaxation is similar but may only be applied to gases for which all species enjoy identical relaxation behavior. Under the same limitations, the derivation for pair-selection appears in Lumpkin *et al.*

A. Fraction of relaxing particles

Consider a gas mixture for which the macroscopic rotational relaxation of species A due to collisions with particles of species B is governed by collision number $Z_{A|B}$ in Jeans' Eq. (15). Likewise, relaxation of species B due to collisions with species A is governed by $Z_{B|A}$. In this mixture, the total relaxation rate of species A is given by the sum of contributions resulting from collisions with all possible partner species B in the gas,

$$\frac{dE_{r_A}}{dt} = \sum_B \frac{E_{r_A}^*(t) - E_{r_A}(t)}{\tau_{c_{A|B}} Z_{A|B}}. \qquad \text{(A1)}$$

In many continuum analyses, the sum over binary collision time constants $\tau_{c_{A|B}} Z_{A|B}$ is often replaced by a molar average over mean collision times; Eq. (A1) is employed in the present work as it is simpler and more general. Note that a new notation is employed in this appendix to facilitate derivation for general gas mixtures. We wish to derive corresponding expressions for DSMC probabilities $P_{A|B}$ and $P_{B|A}$.

In a given collision, the first particle of the pair is tested for relaxation. If accepted, the Borgnakke-Larsen method for collision mechanics is applied for relaxation of this particle only. If rejected, then and only then will the second particle be tested for relaxation which may or may not be accepted. This selection methodology is depicted in the probability tree of Fig. 6. Note that the probability of the first particle being of species A in a given $A+B$ pair is $1/2$, assuming random pairing. From the figure, it is clear that the fraction of collisions for which particle A is the first particle in the pair, and is accepted for relaxation, is $P_{A|B}/2$. The fraction of collisions for which A is the second particle, yet is accepted for relaxaton, is $(1 - P_{B|A})P_{A|B}/2$. Note also that the fraction of accepted collisions equals the fraction of accepted particles for this selection methodology. It follows that the total fraction $F_{A|B}$ of A particles which collide with B particles and experience relaxation is given by the sum

$$F_{A|B} = \frac{1}{2}P_{A|B} + \frac{1}{2}\left(1 - P_{B|A}\right) P_{A|B} \qquad \text{(A2)}$$

$$= P_{A|B}\left(1 - \frac{1}{2}P_{B|A}\right). \qquad \text{(A3)}$$

B. Effect upon ensemble energy

Denote the mean rotational energy of the ensemble of A particles at a given time t in the DSMC simulation by $E_{r_A}^t \equiv E_{r_A}(t)$. In a relaxing $A + B$ collision, the mechanics of Borgnakke-Larsen will lead to an equilibrium division of total mean collision energy $E_T^t + E_{r_A}^t$, where E_T^t is the mean relative translational energy of colliding particles at time t and has $\zeta_T = 4 - 4/\alpha$ DOF near equilibrium. In this model the post-collision rotational energy of those particles at time t which relax during the time step (denoted $E_{r_{A,\mathrm{rlx}}}^{t'}$) is given by the ratio of equilibrium DOF,[22]

$$E_{r_{A,\mathrm{rlx}}}^{t'} = \frac{\zeta_{r_A}}{\zeta_T + \zeta_{r_A}}\left(E_T^t + E_{r_A}^t\right), \qquad \text{(A4)}$$

where ζ_{r_A} is the equilibrium number of rotational DOF for species A.

During a given time step of duration Δt, the total fraction of species A which collide with species B is given by the ratio $\Delta t/\tau_{c_{A|B}}$. Here, $\tau_{c_{A|B}}$ is the collision time for species A given in Eq. (2) when using $n = n_B$ and $\alpha = \alpha_{A,B}$. The mean rotational energy at the end of the time step (denoted $E_{r_A}^{t+\Delta t}$) would include contributions from relaxing particles and from particles unchanged during the time step,

$$E_{r_A}^{t+\Delta t} = \frac{\Delta t}{\tau_{c_{A|B}}} F_{A|B}\, E_{r_{A,\mathrm{rlx}}}^{t'} + \left(1 - \frac{\Delta t}{\tau_{c_{A|B}}} F_{A|B}\right) E_{r_A}^t. \qquad \text{(A5)}$$

Substituting the expression from Eq. (A4) and simplifying leads to

$$E_{r_A}^{t+\Delta t} = \frac{\Delta t}{\tau_{c_{A|B}}} F_{A|B} \frac{\zeta_T}{\zeta_T + \zeta_{r_A}} \left(\frac{\zeta_{r_A}}{\zeta_T} E_T^t - E_{r_A}^t \right) + E_{r_A}^t. \tag{A6}$$

C. Relaxation rate equation

To cast the result of Eq. (A6) into a form representative of Jeans Eq. (15), we note that the DSMC method approximates the rate of rotational energy change as,

$$\frac{dE_{r_A}^t}{dt} \approx \frac{E_{r_A}^{t+\Delta t} - E_{r_A}^t}{\Delta t} \tag{A7}$$

$$= \frac{\zeta_T}{\zeta_T + \zeta_{r_A}} \frac{(\zeta_{r_A}/\zeta_T)\, E_T^t - E_{r_A}^t}{\left(\tau_{c_{A|B}}/F_{A|B}\right)}. \tag{A8}$$

If the ensemble gas is near equilibrium in the translational mode such that molecular velocities are distributed in Maxwellian form, then the relationship between mean translational energy E_t and mean relative translational energy of colliding particles E_T is given by the ratio of DOF,

$$\frac{E_t^t}{E_T^t} = \frac{\zeta_t}{\zeta_T}. \tag{A9}$$

Likewise, the instantaneous equilibrium rotational energy $E_{r_A}^*(t)$ is defined by the expression,

$$E_{r_A}^*(t) = \frac{\zeta_{r_A}}{\zeta_t} E_t^t. \tag{A10}$$

Substituting Eqs. (A9) and (A10) into Eq. (A8) leads to the rate equation

$$\frac{dE_{r_A}^t}{dt} = \frac{\zeta_T}{\zeta_T + \zeta_{r_A}} \frac{E_{r_A}^*(t) - E_{r_A}^t}{\left(\tau_{c_{A|B}}/F_{A|B}\right)}. \tag{A11}$$

By equating terms in (A10) and (A11),

By comparison to Eq. (15), and employing the expression in Eq. (A2), the following relationship results between the macroscopic collision number and the required DSMC probabilities,

$$\frac{1}{Z_{A|B}} = P_{A|B} \left(1 - \frac{1}{2} P_{B|A} \right) \frac{\zeta_T}{\zeta_T + \zeta_{r_A}}. \tag{A12}$$

Note that $Z_{A|B}$ is dependent upon both $P_{A|B}$ and $P_{B|A}$. Substitution of the appropriate indices leads to the corresponding expression for $Z_{B|A}$. When combined, these equations yield a single quadratic expression which may be solved for $P_{A|B}$ in terms of parameters associated with both species A and B,

$$\frac{1}{2} P_{A|B}^2 - \left(\frac{1}{2} \frac{\zeta_T + \zeta_{r_A}}{\zeta_T} \frac{1}{Z_{A|B}} - \frac{1}{2} \frac{\zeta_T + \zeta_{r_B}}{\zeta_T} \frac{1}{Z_{B|A}} + 1 \right) P_{A|B} + \frac{\zeta_T + \zeta_{r_A}}{\zeta_T} \frac{1}{Z_{A|B}} = 0. \tag{A13}$$

A similar relation for $P_{B|A}$ is formed by switching the appropriate indices. The special case of a single-species gas, corresponding to $\zeta_{r_A} = \zeta_{r_B}$ and $Z_{A|B} = Z_{B|A}$, leads to the result cited in Eq. (16). Similarly, collision between a polyatomic molecule ($\zeta_{r_A} \geq 2$) and an atom ($\zeta_{r_B} = 0, Z_{B|A} = \infty$) is equivalent to the pair-selection result cited in Eq. (13).

To demonstrate application of this selection method for a general binary mixture, relaxation of an adiabatic reservoir of species A and B was simulated where all energy was initially in the translational mode only. The reservoir was specified as follows: $n_A/n = 0.3$, $n_B/n = 0.7$, $\alpha = \infty$, $\zeta_{r_A} = 2$, $\zeta_{r_B} = 3$. The relaxation rates and corresponding values of Z, $\tilde{Z}$, and P are specified in Table 1. Results of DSMC simulation permitting double relaxation and using $P = 1/\tilde{Z}$ are plotted in Fig. 7 along with results when prohibiting double-relaxation and using P defined in Eq. (A13). Note that the latter results compare best to those from numerical integration of Jeans Eq. (A1). This serves to validate the selection rule of the present work for gas mixtures.

The only limitation to the analysis above is the assumption in Eq. (A9) that the translational mode is near equilibrium. Rotational energy exchanges which are too frequent during one time step in a relaxing gas may lead to an insufficient number of intermediate elastic collisions, thus preventing the translational mode from equilibrating locally. As a consequence, the assumption in Eq. (A9) may be invalid when the rotational selection probability $P_{A|B}$ approaches unity.

This derivation applies only to the particle-selection methodology which prohibits double-relaxation on one collision. For the methodology which permits double relaxation, or for the pair-selection method, the corresponding expressions for $E_{r_A}^{t+\Delta t}$ could not be reduced to the simple form in Eq. (A11) as required to match Jeans' equation for general gas mixtures. For simple gases in which the rotational modes of all species are assumed equal, the derivation above may be tailored to these other methodologies, leading to the expressions in Eqs. (13) and (14). In those cases, however, one must be careful to employ the correct particle-fractions which may differ from the corresponding collision-fractions.

D. Multimode internal relaxation

If collisions permit simultaneous relaxation of different internal energy modes of a molecule, then the energy relaxation rate equation corresponding to Borgnakke-Larsen mechanics for one mode would include energy terms for the other mode. As such the rate equations could not be cast into the Jeans-Landau-Teller form in Eq. (15). The macroscopic behavior of coupled multimode relaxation is not well understood, and perhaps may not be described correctly by Eq. (15). Nonetheless, to reproduce this macroscopic behavior exactly, one needs simply to prohibit simultaneous relaxation of two energy modes during a single collision. One such selection methodology is depicted in a probability tree in Fig. 8.

Because rotational relaxation of each particle is tested prior to testing for vibrational relaxation in Fig. 8, the resulting rotational probabilities are the same as derived above and described in Eq. (A13). However, expressions for vibrational relaxation probabilities P_v include rotational probability terms P_r and were derived in the same manner used above, leading to

$$\frac{1}{2}\left(1-P_{r_{A|B}}\right)\left(1-P_{r_{B|A}}\right)P_{v_{A|B}}^2 - \left[\frac{1}{2}\frac{\zeta_T+\zeta_{v_A}}{\zeta_T}\frac{\tau_{c_{A|B}}}{\tau_{v_{A|B}}} - \frac{1}{2}\frac{\zeta_T+\zeta_{v_B}}{\zeta_T}\frac{\tau_{c_{B|A}}}{\tau_{v_{B|A}}} + \left(1-P_{r_{A|B}}\right)\left(1-P_{r_{B|A}}\right)\right]P_{v_{A|B}} + \frac{\zeta_T+\zeta_{v_A}}{\zeta_T}\frac{\tau_{c_{A|B}}}{\tau_{v_{A|B}}} = 0. \tag{A14}$$

Here, $\tau_{v_{A|B}}$ refers to the characteristic vibrational relaxation time in the Landau-Teller rate equation and has been measured experimentally by Millikan and White[32] and Camac[33] for several gases. The effective DOF ζ_v reflects the vibrational energy content and is dependent upon flowfield temperature.[14,24]

Switching the appropriate indices in Eq. (A14) leads to the corresponding expression for $P_{v_{B|A}}$. Note that the selection order in the methodology of Fig. 8 could be rearranged freely, leading to different probability expressions which are nonetheless similar to those in Eqs. (A13) and (A14).

REFERENCES

[1] G.A. Bird, *Molecular Gas Dynamics* (Clarendon Press, Oxford, 1976).

[2] G.A. Bird, *Molecular Gas Dynamics and the Direct Simulation of Gas Flows* (Clarendon Press, Oxford, 1994).

[3] K. Nanbu, "Direct simulation scheme derived from the Boltzmann equation. I. Monocomponent gases," *J. Phys. Soc. Japan* **49**, 2042 (1980).

[4] K. Koura, "Null-collision technique in the direct simulation Monte Carlo technique," *Phys. Fluids* **29**, 3509 (1986).

[5] D. Goldstein, B. Sturtevant, and J. E. Broadwell, "Investigations of the motion of discrete-velocity gases," in *Rarefied Gas Dynamics: Theoretical and Computational Techniques*, Progress in Astronautics and Aeronautics, edited by E. P. Muntz, D. P. Weaver, and D. H. Campbell (AIAA, Washington, DC, 1988), Vol. 118, p. 100.

[6] F. Gropengießer, H. Neunzert, and J. Struckmeier, "Computational methods for the Boltzmann equation," in *The State of the Art in Applied and Industrial Mathematics*, edited by R. Spigler (Kluwer Academic Publishers, Dordrecht, 1990).

[7] M. S. Ivanov, and S. V. Rogasinsky, "Theoretical analysis of traditional and modern schemes of the DSMC method," in *Rarefied Gas Dynamics*, Proceedings of the 17th International Symposium on Rarefied Gas Dynamics, edited by A. E. Beylich (VCH, Weinheim, 1991), p. 629.

[8] D. Baganoff and J.D. McDonald, "A collision-selection rule for a particle simulation method Suited to Vector Computers," *Phys. Fluids A* **2**, 1248 (1990).

[9] I.D. Boyd, "Rotational-translational energy transfer in rarefied nonequilibrium flows," *Phys. Fluids A* **2**, 447 (1990).

[10] T. Abe, "New model of DSMC for internal-translational energy transfer in nonequilibrium flow," Presented at the 18th International Symposium on Rarefied Gas Dynamics, Vancouver, July (1992).

[11] K. Koura, "Statistical inelastic cross-section model for the Monte Carlo simulation of molecules with continuous internal energy," *Phys. Fluids A* **5**, 778 (1993).

[12] I.D. Boyd, "Analysis of vibrational-translational energy transfer using the direct simulation Monte Carlo method," *Phys. Fluids A* **3**, 1785 (1991).

[13] B.L. Haas, "Thermochemistry models applicable to a vectorized particle simulation," Ph.D. Thesis (Department of Aeronautics and Astronautics, Stanford University, 1990).

[14] B.L. Haas, J.D. McDonald, and L. Dagum, "Models of thermal relaxation mechanics for particle simulation methods," *J. Comput. Phys.*, (in press) (1993).

[15] F. Bergemann and I.D. Boyd, "DSMC simulation of inelastic collisions using the Borgnakke-Larsen method extended to discrete distributions of vibrational energy," Presented at the 18th International Symposium on Rarefied Gas Dynamics, Vancouver, July (1992).

[16] B.L. Haas, "Models of energy-exchange mechanics applicable to a particle simulation of reactive flow," *J. Thermophys. Heat Transfer* **6**, 200 (1992).

[17] B.L. Haas and I.D. Boyd, "Models for direct Monte Carlo simulation of coupled vibration-dissociation," *Phys. Fluids A* **5**, 478 (1993).

[18] D. B. Hash, and H. A. Hassan, "Direct simulation with vibration-dissociation coupling," *J. Thermophys. Heat Transfer* (in press) (1993).

[19] G.A. Bird, "A new chemical reaction model for DSMC Studies," Presented at the 18th International Symposium on Rarefied Gas Dynamics, Vancouver, July (1992).

[20] S. Dietrich, "Improved DSMC modeling of near-continuum flows with chemical reactions," Presented at the 18th International Symposium on Rarefied Gas Dynamics, Vancouver, July (1992).

[21] C. Borgnakke and P.S. Larsen, "Statistical collision model for Monte Carlo simulation of polyatomic gas mixture," *J. Comput. Phys.* **18**, 405 (1975).

[22] F.E. Lumpkin III, B.L. Haas, and I.D. Boyd, "Resolution of differences between collision number definitions in particle and continuum simulations," *Phys. Fluids A* **3**, 2282 (1991).

[23] J.H. Jeans, *The Dynamical Theory of Gases* (Cambridge U.P., London, 1916). ← FEL[III] Check Date?

[24] W.G. Vincenti and C.H. Kruger, *Introduction To Physical Gas Dynamics* (Wiley, New York, 1965).

[25] G.A. Bird, "Monte-Carlo simulation in an engineering context," in *Rarefied Gas Dynamics*, edited by S. S. Fischer (AIAA, New York, 1981), Part I, p. 239.

[26] C.H. Chung, S.C. Kim, R.M. Stubbs, K.J. DeWitt, "DSMC and continuum analyses of low-density nozzle flow," AIAA Paper No. 93-0727 (Reno 1993).

[27] E.H. Carnevale, C. Carey, G. Larsen, "Ultrasonic determination of rotational collision numbers and vibrational relaxation times of polyatomic gases at high temperatures," *J. Chem. Phys.* **47**, 2829 (1967).

[28] G.A. Bird, "Definition of mean free path for real gases," *Phys. Fluids* **26**, 3222 (1993).

[29] S. Chapman and T. G. Cowling, *The Mathematical Theory of Non-Uniform Gases* (Third Edition, Cambridge University Press, Cambridge, 1970. p. 173).

[30] J.G. Parker, "Rotational and vibrational relaxation in diatomic gases," *Phys. Fluids* **2**, 449 (1959).

[31] J.A. Lordi and R.E. Mates, "Rotational relaxation in nonpolar diatomic gases," *Phys. Fluids* **13**, 291 (1970).

[32] R.C. Millikan and D.R. White, "Systematics of vibrational relaxation," *J. Chem. Phys.* **39**, 3209 (1963).

[33] M. Camac, "O_2 Vibrational relaxation in oxygen-argon mixtures," *J. Chem. Phys.* **34**, 448 (1961).

TABLE 1: Relaxation rate parameters for simulated mixture

$i\|j$ [a]	Z	$\tilde{Z}$	$1/P$ [b]
A|A	6	3.6	3.4142
A|B	8	4.8	4.9876
B|A	15	7.5	7.7122
B|B	20	10.0	10.9045

[a] Denotes relaxation of species i via collisions with species j.
[b] From Eq. (A13).

FIGURE CAPTIONS

Fig. 1 Solutions of Jeans' Eqs (1) and (3) for hard-sphere and maxwell molecules, using collision numbers related by Eq. (8). a) Results plotted against time normalized by the initial τ_c. b) Results plotted against the cumulative number of collisions $\tilde{t}$ defined in Eq. (10).

Fig. 2 Ratio of P from Eq. (14) to $1/\tilde{Z}$, derived for several VHS intermolecular potentials, α, corresponding to the particle-selection methodologies for which double relaxation is permitted in a diatomic gas ($\zeta_r = 2$).

Fig. 3 Diatomic rotational energy during relaxation in an adiabatic reservoir ($\tilde{Z} = 10$). DSMC results used the particle-selection methodology permitting double-relaxation with P defined from: a) $1/\tilde{Z}$, and b) Eq. (14).

Fig. 4 Diatomic rotational energy during relaxation in an adiabatic reservoir ($\tilde{Z} = 10$). DSMC results used the pair-selection methodology with P defined from: a) $1/\tilde{Z}$, and b) Eq. (13).

Fig. 5 Diatomic rotational energy during relaxation in an adiabatic reservoir ($\tilde{Z} = 10$). DSMC results used the particle-selection methodology prohibiting double-relaxation with P defined from: a) $1/\tilde{Z}$, and b) Eq. (16).

Fig. 6 Probability decision tree for the particle-selection methodology prohibiting double-relaxation. Joint probabilities for all possible outcomes are determined on the far right.

Fig. 7 Rotational energy during relaxation of an adiabatic reservoir of the binary gas mixture described in Table 1; comparison between solution of Jeans Eq. (A1) and DSMC simulation, a) permitting double relaxation and using $P = 1/\tilde{Z}$, and b) prohibiting double relaxation and using P defined from Eq. (A13). The time axis is normalized by the initial value of $\tau_{c_{A|A}}$.

Fig. 8 Probability decision tree for rotational and vibrational relaxation using a particle-selection methodology which prohibits multiple relaxation events per collision.

Fig. 1
Haas, et al.
Physics of Fluids A

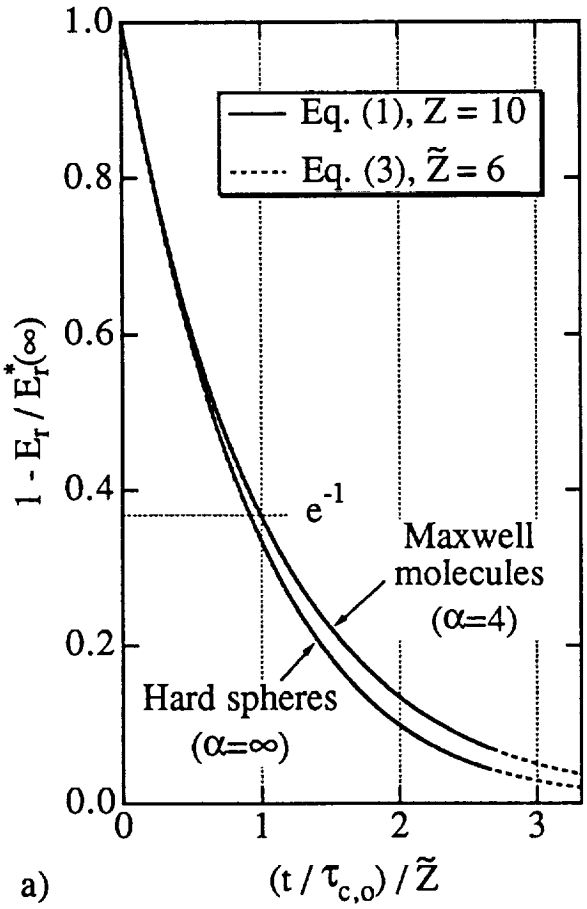

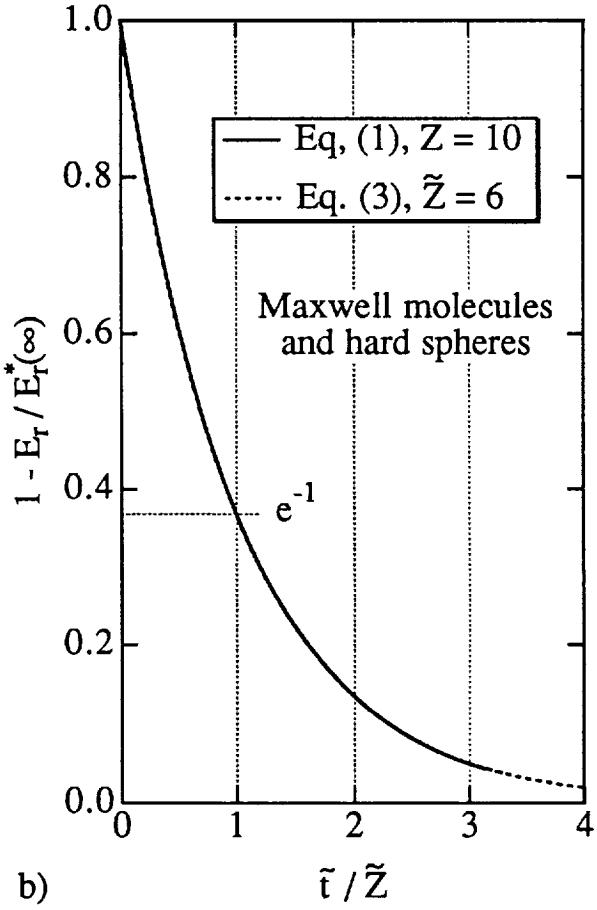

/rot/Figs/misc/J&BEqu.igr

Fig. 2
Haas, et al.
Physics of Fluids A

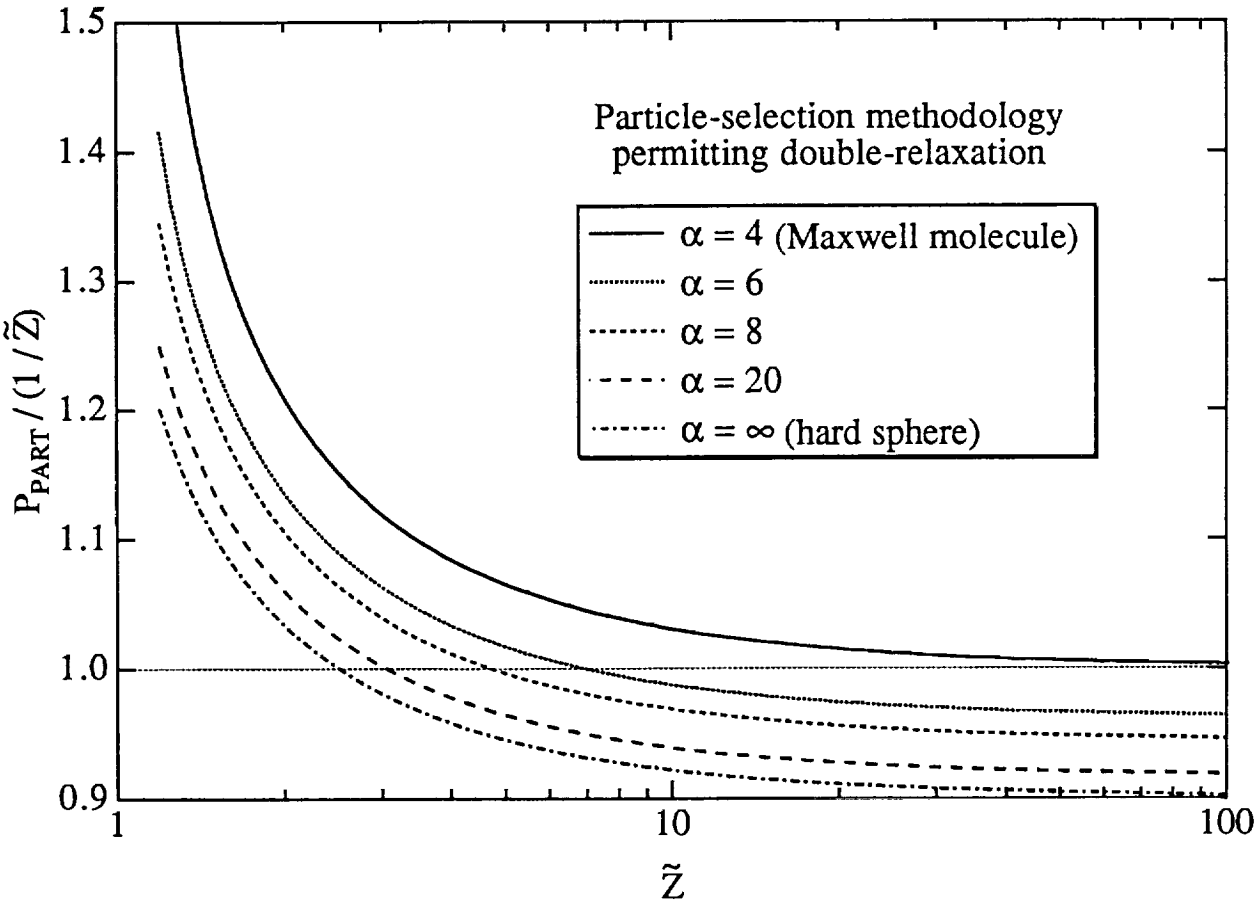

/rot/figs/ZPratio.igr

Fig. 3
Haas, et al.
Physics of Fluids A

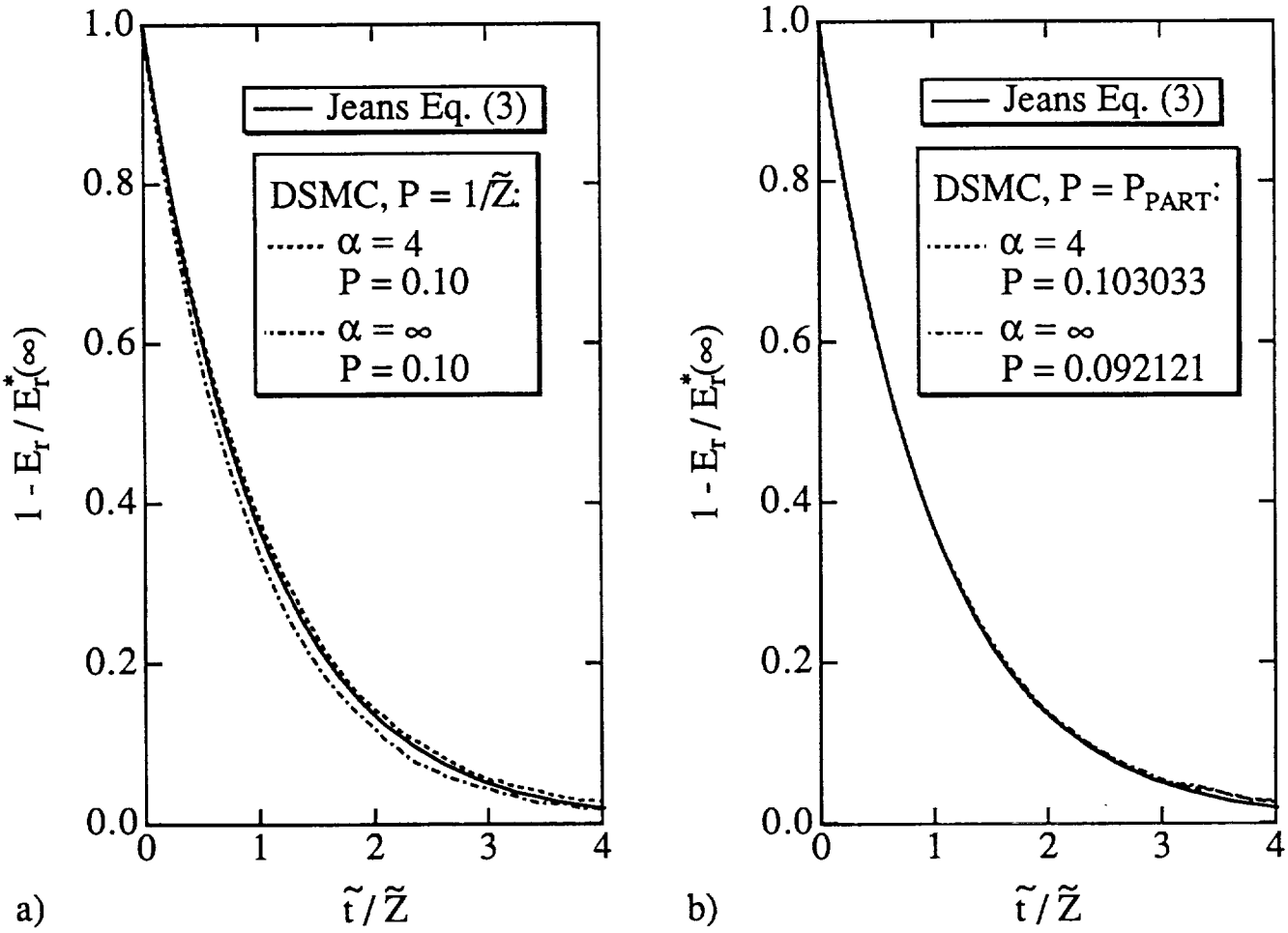

/rot/Figs/RlxDPart/DPart.igr

Fig. 4
Haas, et al.
Physics of Fluids A

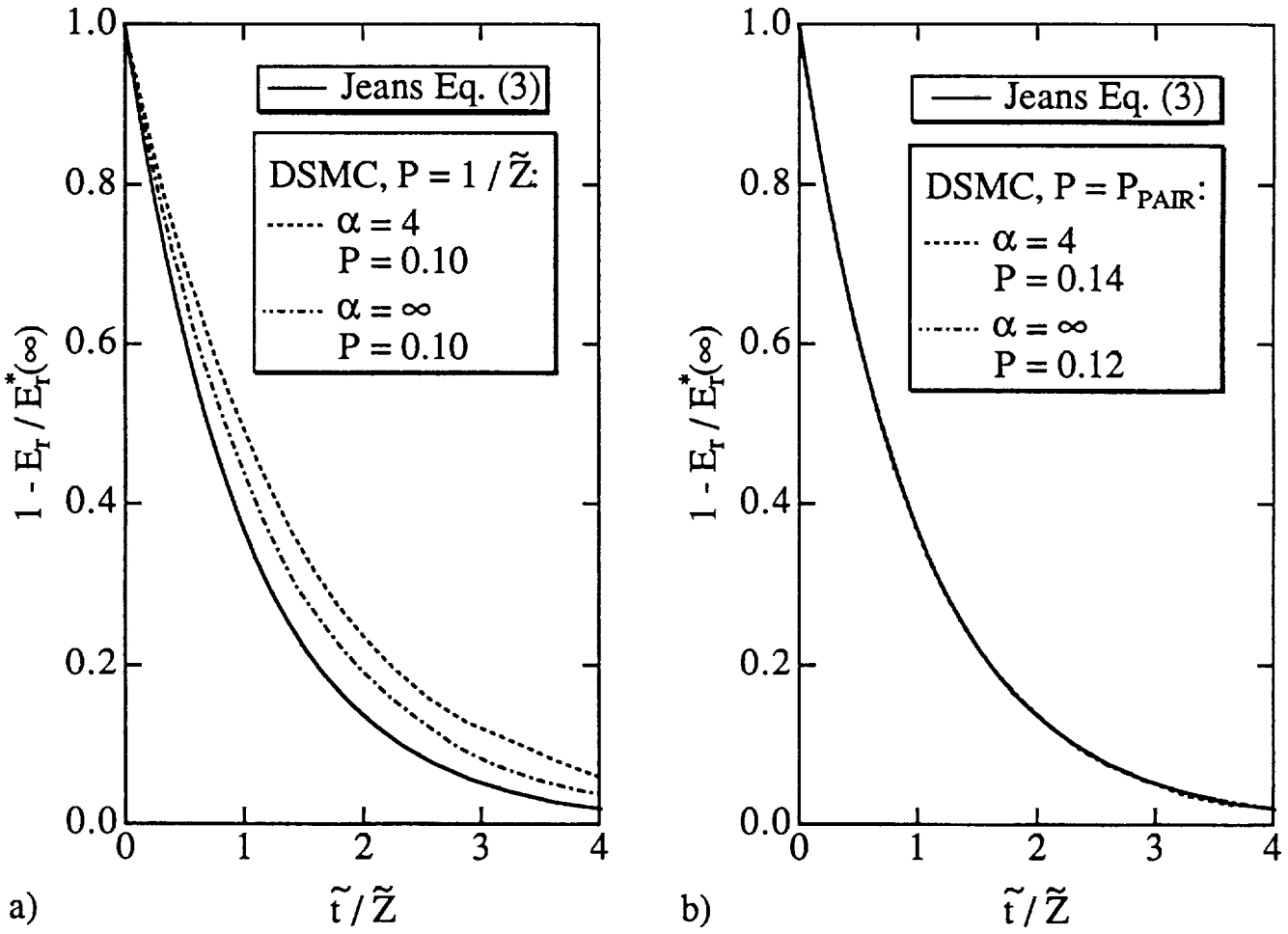

/rot/Figs/RlxPair/Pair.igr

Fig. 5
Haas, et al.
Physics of Fluids A

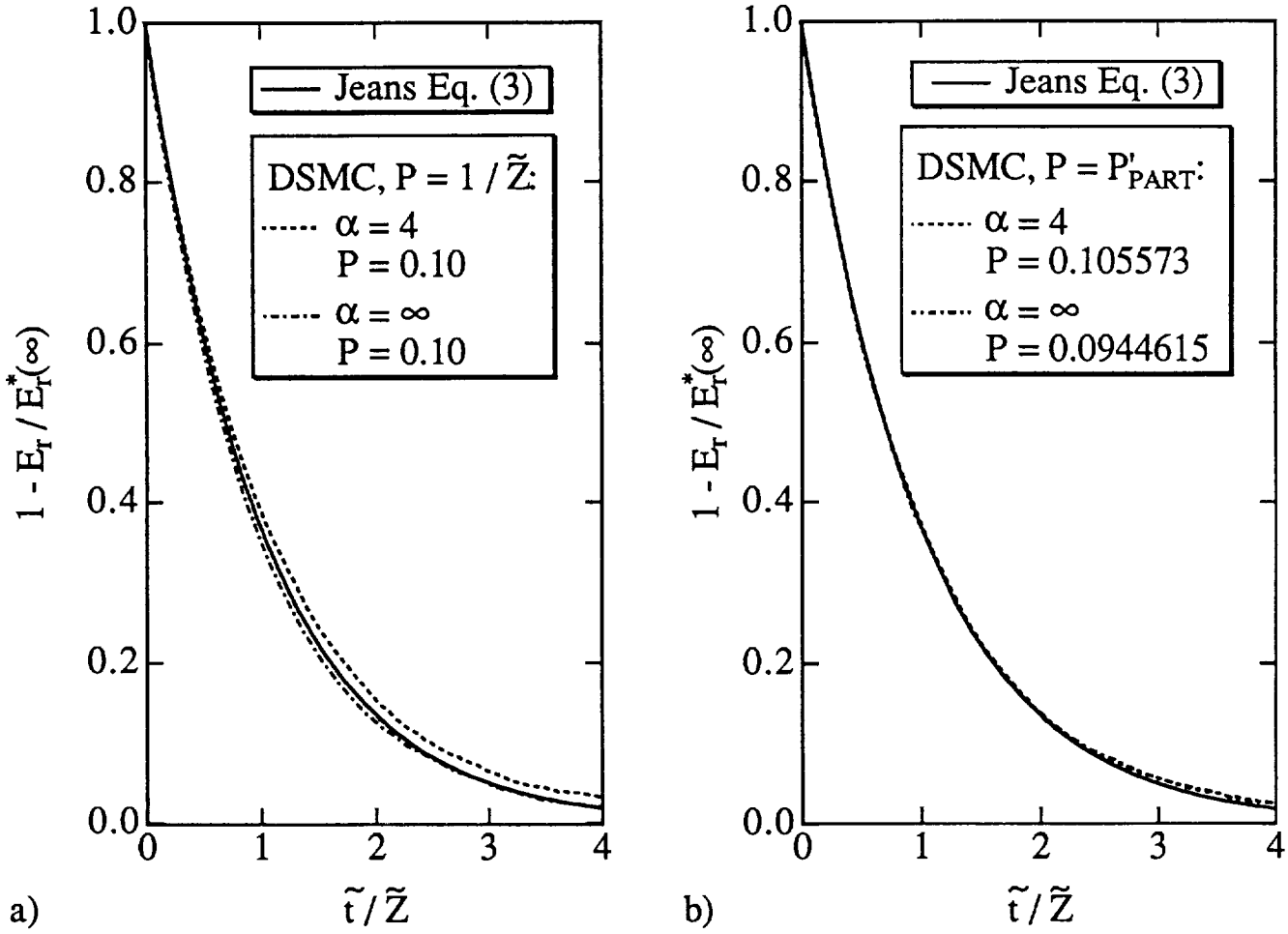

/rot/Figs/RlxSPart/Spart.igr

Fig. 6
Haas, et al.
Physics of Fluids A

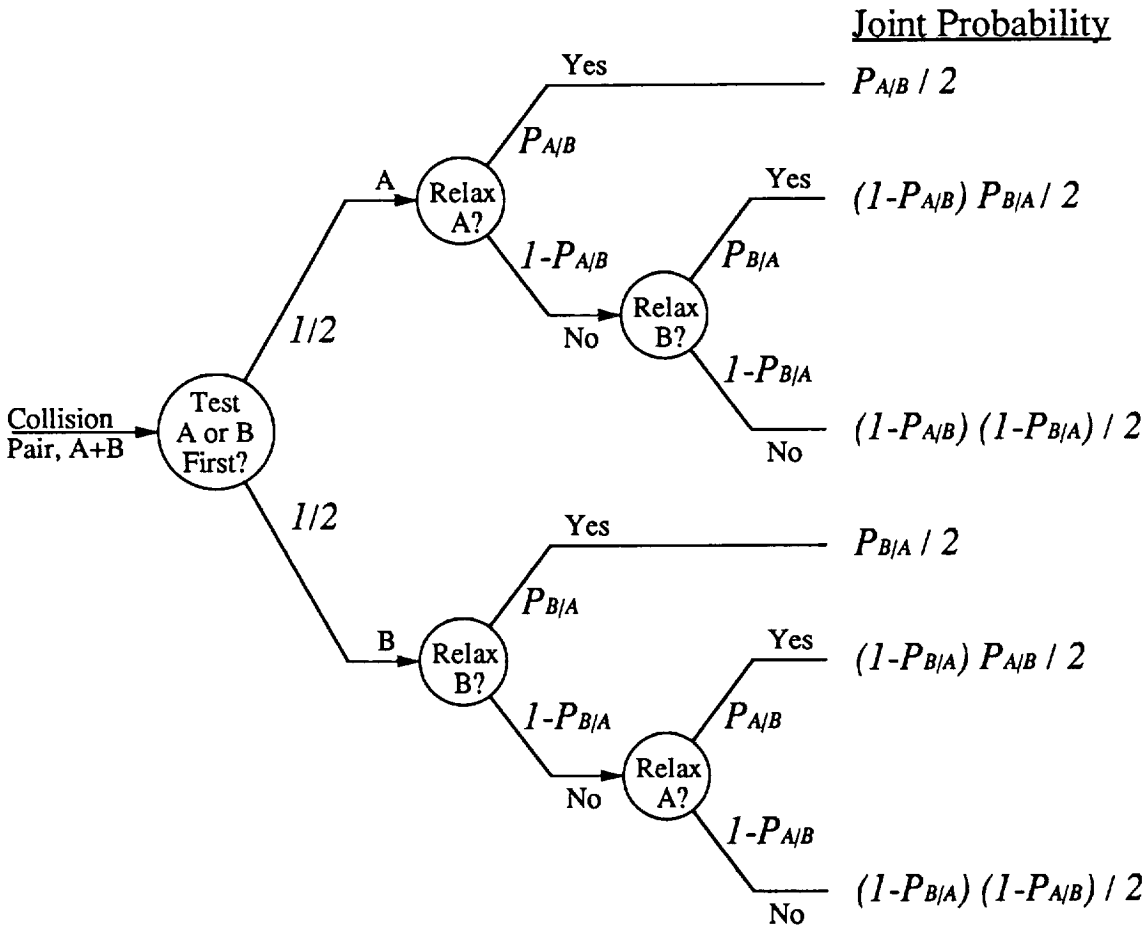

/rot/Figs/misc/SPartPTree.drw

Fig. 7
Haas, et al.
Physics of Fluids A

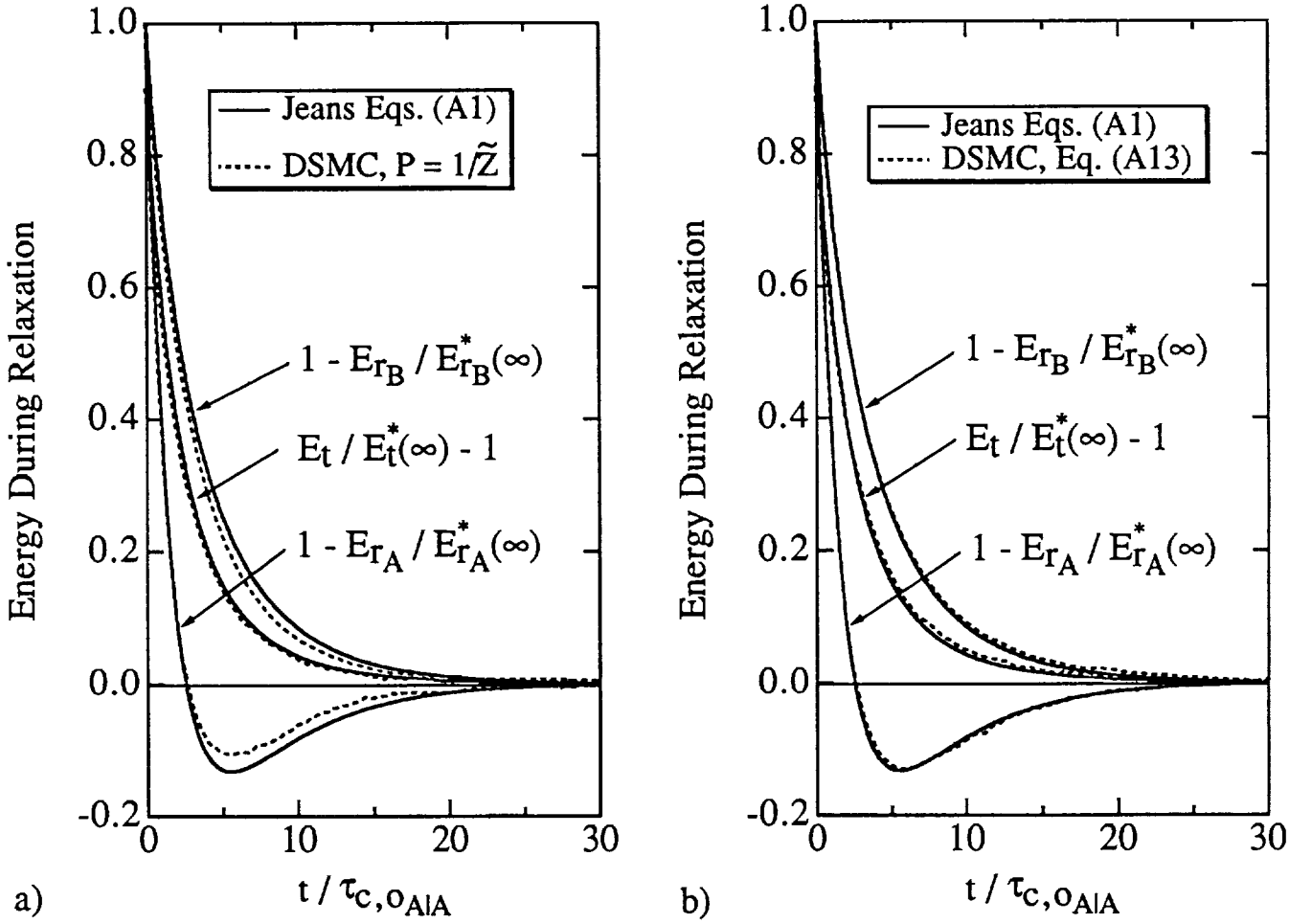

/rot/Figs/RlxMix/Mix.igr

Fig. 8
Haas, et al.
Physics of Fluids A

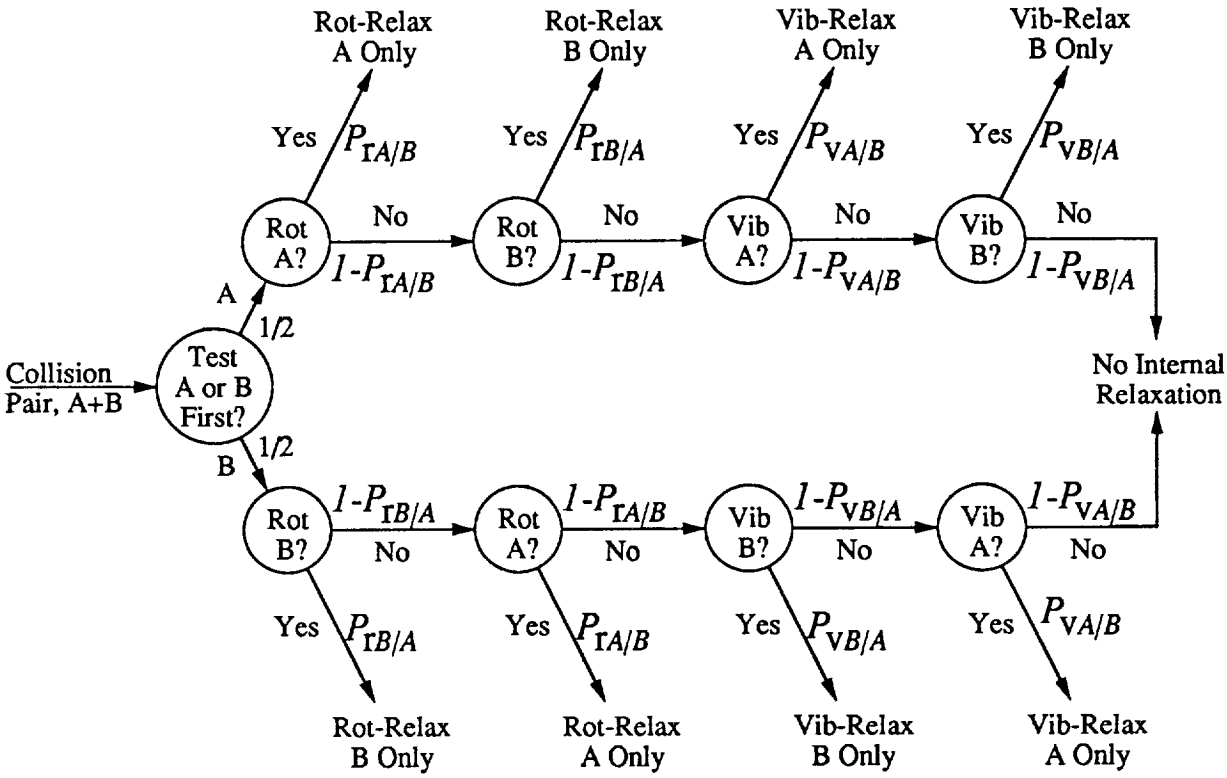

/rot/Figs/misc/MixPTree.drw

Appendix B

AIAA 93-2765

Models for Dynamic Surface Temperatures During Rarefied Aeropass Maneuvers

Brian L. Haas
Eloret Institute
Palo Alto, CA 94303

AIAA 28th Thermophysics Conference
July 6-9, 1993 / Orlando, FL

Models for Dynamic Surface Temperatures During Rarefied Aeropass Maneuvers

Brian L. Haas*
Eloret Institute, Palo Alto, California 94303

Models are developed to compute surface temperatures in a direct simulation Monte Carlo (DSMC) particle method for vehicles during atmospheric entry. This involves time-integration of the governing heat transport equations over the duration of the time-dependent heating pulse, and then coupling these temperatures into the DSMC solution. This model is adapted specifically for application to thin panels in highly-rarefied flows and yields the transient thermal response of individual surface facets by accounting for radiative emission, thermal conductivity, and material heat capacity. The model may be simpified for materials with instant thermal response due to negligible heat capacity. Simulation results for radiating panels with internal conductivity are validated by comparison to corresponding free molecule theory. These models are robust, contribute negligible additional computational burden, and permit calculation of all surface-facet temperatures independently. Furthermore, these models may be used in continuum methods for computational fluid dynamics. Sensitivity of aerodynamic heating, drag, and lift to surface temperature is assessed through simulations of several hypersonic rarefied flows past flat panels at 45° incidence.

Nomenclature

A	thermal accommodation coefficient
C	aerodynamic force coefficients
c	effective material heat capacity (J/m^{2}K)
E	error residuals for Newton iteration
H	flow similarity parameter, Eq. (14)
k	Boltzmann constant, 1.3805×10^{-23} J/K
Kn	Knudsen Number
M	Mach number
n	gas number-density (m^{-3})
q	transient net convective heat flux
Q	net convective heat flux computed in DSMC
S	speed ratio, $S = \sqrt{\gamma/2}\mathrm{M}_\infty$
T	temperature
$\overline{T}$	temperature normalization parameter, Eq. (4)
t	time during heating pulse
Z	number flux parameter, Eq. (17)
α	exponent of intermolecular potential
β	angle of incidence of panel to free-stream flow
γ	ratio of specific heats
ε	material radiative emissivity
ζ_{int}	molecular internal degrees of freedom ($\zeta_{int} = 2$)
η	temperature similarity parameter, Eq. (15)
κ	effective thermal conductivity (W/m^{2}K)
ρ	gas mass-density (kg/m^3)
σ	Stefan-Boltzmann const., 5.67×10^{-8} W/(m^{2}K^4)
τ	heating pulse time-constant, perigee at $t = \tau$
ω	molecule translational energy-flux, Eq. (16)

Subscripts:

a, b	front,back-side of panel
D	drag or deep-space value
L	lift
o	stagnation value
i, j	value at surface node, neighboring node
w	value at wall or surface
∞	freestream value

Introduction

To perform orbital maneuvers in a manner which expends little onboard fuel, spacecraft may pass through the outer reaches of planetary atmospheres. Such scenarios are characterized by extremely rarefied flows at high velocities with transient heat fluxes to vehicle surfaces. However, delicate spacecraft components such as solar panels may not withstand severe aerodynamic heating or body loading. Accurate prediction of the rarefied flow field and subsequent vehicle aerodynamics is therefore essential to successful mission planning for aeropass maneuvers. One contemporary example of such a scenario is the aerobraking of the Magellan spacecraft to circularize its highly eccentric orbit about Venus.[1] Magellan's solar panels, which are mounted normal to the flow direction, place severe restrictions on the acceptable flight altitudes and body torques during each aeropass. More importantly, non-zero material heat capacity and finite conductivity through the panels lead to transient surface temperatures during the short heat pulse of aerobraking.

Highly rarefied flows, for which the ratio of molecular

* Research Scientist, Aerothermodynamics Branch. Member, AIAA. Mailing Address: NASA Ames Research Center, M/S 230-2, Moffett Field, CA 94035-1000.

mean free path to a body dimension is large (Knudsen number, Kn>0.10), are best simulated computationally with direct simulation Monte Carlo (DSMC) particle methods.[2,3] Here, gas dynamics is modeled directly by the motion and interaction of thousands or millions of discrete particles. Particles which strike the vehicle may reflect back into the flow with velocities and internal energies corresponding to full or partial accommodation to surface. In rarefied flows, molecular diffusion from vehicle surfaces affects the incoming flow. Therefore, surface temperatures play a significant role in establishing the net heat transfer to the body. More importantly, aerodynamic body forces perpendicular to the freestream direction depend only upon the flux of particles away from the surface. Since this efflux is itself greatly dependent upon surface temperature, the net aerodynamics of a vehicle in rarefied flows exhibits tremendous sensitivity to surface temperatures as well.

The objectives of the present work are two-fold. The first goal is to assess the sensitivities of aerodynamic heating and forces to surface temperature for several blunt-body entry flows. The second goal is to develop new models which calculate dynamic surface temperatures directly in the particle simulation rather than requiring the use of prescribed isothermal estimates. These models account for the radiative emissivity, thermal conductivity, and heat capacity of the material. These heat-transport properties are particularly important for atmospheric entry heating pulses of short duration in which transient temperature profiles lead to peak temperatures occurring after the peak heating point because of non-zero heat capacity of the material. Simplifing the dynamic model for materials with negligible heat capacity permits validation of the methods through comparison to theoretical predictions in free molecular flows. Although models of this type have been demonstrated for application to ordinary single-sided surfaces,[4] the present study will address application to thin panels which have dynamic temperatures on both front and back sides.

Aerodynamic Sensitivity to Surface Temperature

For a simple assessment of aerodynamic sensitivity to surface temperatures, steady-state rarefied flow past a flat thin plate was simulated with the DSMC technique using a computationally efficient code.[5] The two-dimensional simulation geometry as used throughout the present work is depicted in Fig. 1. The pitch angle was fixed at $\beta = 45°$ and the intermolecular potential in the diatomic gas[3] was described by $\alpha = 8$. The rotational collision number was set to unity while that for vibration was set to zero in order to maintain a fixed number of internal degrees of freedom of two and a constant ratio of specific heats, $\gamma = 1.4$. Flow conditions were varied as follows,

$$\mathrm{Kn}_\infty = \{1, 10, \infty\}$$

$$\mathrm{M}_\infty = \{5, 10, 20\}$$

$$T_w/T_\infty = \{1, 2, 4, 8, 16\}$$

In these simulations, the wall temperature was fixed at prescribed value T_w over the entire plate surface. Reflection from the surface was fully diffuse and thermally accommodated ($A = 1.0$). Figure 2 depicts the dependence of the steady-state net convective heat transfer Q upon T_w. Note that the ratio $Q(T_w)/Q(T_\infty)$ is independent of Kn_∞. Note also that the curves are nearly identical at all Mach numbers when surface temperature is normalized by the total (stagnation) temperature, T_o. Dependence of heating upon M_∞ is therefore described by the standard isentropic expression for T_o,

$$\frac{T_o}{T_\infty} = 1 + \frac{\gamma - 1}{2}\mathrm{M}_\infty^2 .$$

It follows that the dependence of Q upon T_w diminishes with increased M_∞, regardless of flow-field rarefaction, Kn_∞.

Sensitivity of plate drag to surface temperature is demonstrated in Fig. 3. Just as with heating, drag sensitivity is nearly identical for all Kn_∞, but depends strongly upon M_∞. In general, drag is marginally sensitive to wall temperature, changing by less than a factor of two over the range of T_w studied here.

Lift coefficients are more sensitive to T_w as demonstrated in Fig. 4. Unlike heating and drag, lift depends greatly upon Kn_∞. For example, at $\mathrm{Kn}_\infty = 1$, the curves for lift are similar, although slightly higher in magnitude, than those for drag. But as flow rarefaction increases, sensitivity to T_w increases, and the distinction between the curves at each M_∞ begins to diminish. Indeed, these simulation results agree with free molecular flow theory[6] which predicts the following dependence,

$$C_L \sim S^{-2}\left[\mathrm{erf}\,(\beta S) + \sqrt{\pi T_w/T_\infty}\,\beta S\right].$$

As demonstrated here, heating, drag, and especially lift are sensitive to surface temperature in hypersonic rarefied flows. Use of inaccurate estimates of T_w in simulations of these flows could lead to unreliable aerodynamic predictions.

Model for Dynamic Surface Temperatures

For rarefied entry flows about thin panels, a new model is employed in the present work which couples the surface heat transfer into the flow solution to compute dynamic surface temperatures directly rather than prescribe some estimated constant temperature profile to the vehicle. A panel surface is composed of individual planar facets, each modeled with a thermal node on the front and back sides. Each

node i has an associated heat capacity c_i, temperature $T_i(t)$, radiating emissivity ϵ_i, and dynamic net convective heat flux $q_i(t)$ per unit area; and is connected to neighboring nodes j with conductivity $\kappa_{i,j}$. The corresponding energy balance for each node i is given by

$$q_i(t) - \varepsilon_i \sigma \left(T_i^4 - T_D^4\right) - \sum_j \kappa_{i,j} \left(T_i - T_j\right) = c_i \frac{dT_i}{dt}, \quad (1)$$

where T_D is the deep-space temperature. Coefficients c and κ are written in a form which already accounts for material thicknesses and densities.

For practical application to thin panels in the present work, we replace the general "i, j" network in Eq. (1) with independent dual-node surface facets. That is, thermal conductivity is considered only through the panel from front (side "a") to back (side "b") of a given facet, and is neglected laterally along the panel surface from facet to facet. Furthermore, at all but the smallest incidence angles β for panels in rarefied flow, convective heat flux on the back side may be neglected ($q_b \rightarrow 0$). These assumptions lead to the following set of coupled equations which represent a dual-node model for the thermal characteristics of a thin panel surface facet in hypersonic rarefied flows,

$$\begin{aligned} q_a(t) - \varepsilon_a \sigma \left(T_a^4 - T_D^4\right) - \kappa \left(T_a - T_b\right) &= c_a \frac{dT_a}{dt} \\ -\varepsilon_b \sigma \left(T_b^4 - T_D^4\right) + \kappa \left(T_a - T_b\right) &= c_b \frac{dT_b}{dt}. \end{aligned} \quad (2)$$

This model may be applied regardless of the assumed thermal accommodation coefficient or surface reflection model (diffuse versus specular, *etc.*). Furthermore, a unique set of equations (2) may be written for each surface facet independently. Note that q represents the *net* convective energy flux, accounting for both incident and reflected molecular energies. The peak value Q for the net heat flux is simply measured directly in the DSMC code for each facet, and it accounts for any contributions of both translational and internal energy modes to gas-surface interaction.

When considering Eqs. (1) or (2), it is important to distinguish time t during the aerobraking maneuver from the time-steps employed in a DSMC method. Note that the DSMC method typically simulates flow at a single instant in time only; say, at the perigee point, τ, where peak heating occurs. Although the method will likely require several averaging-steps to yield a statistically meaningful solution, it nonetheless simulates the flow at a single instant during aerobraking. Equations (2) are coupled into the DSMC code by first assigning some initial temperature profile over the vehicle surface, and measuring the net energy flux Q for each facet after one step. Then, by assuming a time-dependent form for the heating pulse, $q(t)$, with peak value Q, Eqs. (2) may be integrated over t during aerobraking to solve for the dynamic surface temperatures $T_a(t)$ and $T_a(t)$, and thus for the temperatures at perigee, $T_a(\tau)$ and $T_b(\tau)$. The front-side temperature $T_a(\tau)$ is then reassigned to the surface facet for use in the next DSMC step. After several steps, the coupling of this time-interation procedure with the DSMC method improves the estimates for Q and $T_a(\tau)$ simultaneously.

Fortunately, the computational penalty associated with this procedure is negligible in comparison to computation of particle motion and interaction on each simulation step. Again, this procedure is not limited to thin panels, but may be applied readily to single-sided body surfaces.[4]

Application of Coupled Models

Certain parameters in Eqs. (2) may dominate others to yield unique surface thermal characteristics. For example, if the heat capacities are extremely large, then the surfaces are effectively isothermal; such was the condition under which the temperature-sensitivity studies were performed above. If heat capacities are extremely small, then the panel becomes a conducting, double-sided radiator with instant thermal response to the dynamic heat flux. This condition still couples the surface thermal model to the flow-field simulation, and will prove helpful in validating these models through comparison of free molecular predictions to theory.

Perfect Conductors in Radiative Equilibrium

If the heat capacity of the material is negligible ($c \rightarrow 0$), then the panel exhibits instant thermal response to the heat flux. Consequently, surface temperatures for each facet may be assessed by replacing the transient flux $q(t)$ by the steady flux measured in the DSMC code, Q. Furthermore, when the thermal conductivity is large ($\kappa \rightarrow \infty$), then surface temperatures on both sides of the panel must be equal ($T_a = T_b$). The surface facet therefore comes a double-sided node in radiative equilibrium with deep space, and Eqs. (2) reduce to a single analytic equation given by

$$Q = \left(\varepsilon_a + \varepsilon_b\right) \sigma \left(T_a^4 - T_D^4\right). \quad (3)$$

Note that surfaces with zero thermal conductivity (perfect insulators) may be modeled by neglecting the radiative emission of the back side (setting $\epsilon_b = 0$).

To apply the model to a DSMC code, one must first assign some initial surface temperature to each surface facet. During a given simulation step, sample the net convective heat flux Q for each facet and update T_a by solving Eq. (3) for each. This procedure is stable and introduces negligible additional computational burden even when computing T_a for every surface facet after each DSMC step. More importantly, this procedure computes the temperature for each

facet independently and yields accurate surface temperature profiles which are consistent with the assumptions inherent to Eq. (3). This model was used in simulating aerobraking of the Magellan spacecraft.[7] A similar, though considerably more cumbersome model has been suggested by Carey.[8]

To validate this coupled model, steady free molecular flow was simulated with the DSMC technique about flat panels at several flow conditions and angles of incidence. Simulation predictions of surface temperature were compared to those from free molecule theory[9] for perfect conductors in radiative equilibrium. Note that surface heating and temperature are uniform across the entire planar panel in free molecule flows. Simulation conditions are described by all combinations of the following parameters,

$$\begin{aligned} M_\infty &= \{5, 12, 20\} & \varepsilon_{a,b} &= 0.80 \\ \beta &= \{5^\circ, 15^\circ, 30^\circ, 45^\circ, 60^\circ, 90^\circ\} & A &= 1.0 \\ \rho_\infty &= 3.72 \times 10^{-8}\ \mathrm{kg/m^3} & \gamma &= 1.4 \end{aligned}$$

These cases were repeated using a thermal accommodation coefficient of $A = 0.5$ at Mach number $M_\infty = 15$. Results are plotted in Fig. 5 and show excellent agreement for all cases. The following similarity parameter was used to normalize the surface temperature[9]

$$\overline{T} = \left[\sqrt{\frac{2}{\rho_\infty}} \frac{A}{\varepsilon\sigma} \left(n_\infty k T_\infty \right)^{3/2} S^2 \right]^{1/4}. \tag{4}$$

These results verify that the thermal model not only computes the correct temperature, but also that the temperature is coupled appropriately to yield the correct heating rate.

Finite Conductors in Radiative Equilibrium

Returning to Eqs. (2) with finite thermal conductivity through the panel, but maintaining zero heat capacities, yields a set of coupled quartic polynomials which may be solved for T_a and T_b for each double-sided surface facet after each DSMC step. Again, the instant thermal response of the material permits replacing $q(t)$ by Q measured in the DSMC code for each facet. Solution of the coupled polynomials is accomplished most easily through two-variable Newton iteration which involves solution of the vector equation,

$$\frac{\partial \mathbf{E}}{\partial \mathbf{T}} \delta \mathbf{T} = -\mathbf{E} \tag{5}$$

where the error residuals E and their derivatives are defined from Eq. (2) as follows,

$$E_a = Q - \varepsilon_a \sigma \left(T_a^4 - T_D^4 \right) - \kappa \left(T_a - T_b \right) \tag{6}$$

$$E_b = -\varepsilon_b \sigma \left(T_b^4 - T_D^4 \right) + \kappa \left(T_a - T_b \right) \tag{7}$$

$$\partial E_a / \partial T_a = -4 \varepsilon_a \sigma T_a^3 - \kappa \tag{8}$$

$$\partial E_b / \partial T_b = -4 \varepsilon_b \sigma T_b^3 - \kappa. \tag{9}$$

The solution of Eq. (5) for one iteration leads to improved temperature estimates T' as follows,

$$\delta T_a = \frac{\kappa E_b - E_a \left(\partial E_b / \partial T_b \right)}{\left(\partial E_a / \partial T_a \right) \left(\partial E_b / \partial T_b \right) - \kappa^2} \tag{10}$$

$$\delta T_b = -\frac{E_b + \kappa \delta T_a}{\left(\partial E_b / \partial T_b \right)} \tag{11}$$

$$T_a' = T_a + \delta T_a \tag{12}$$

$$T_b' = T_b + \delta T_b. \tag{13}$$

The iteration procedure involves using initial temperature estimates T_a and T_b to evaluate E_a, E_b, $\partial E_a / \partial T_a$, and $\partial E_b / \partial T_b$, and then computing improved estimates T_a' and T_b'. Although this process could be repeated many times per DSMC time-step to yield accurate solutions, several such iterations are not necessary. Rather, performing only one Newton iteration step during each DSMC step will suffice; successive DSMC steps will rapidly drive the surface temperatures to their correct values. That is, as the DSMC solution progresses, the statistical results for Q improve as do the estimates for T_a and T_b per facet.

This Newton iteration process is demonstrated in Fig. 6 which plots the evolution of T_a and T_b during the simulation for free molecule flow of N_2 past a radiating, conducting, panel with conditions specified as follows,

$$\begin{aligned} M_\infty &= 20 & \kappa &= 20\ \mathrm{W/m^2K} \\ \gamma &= 1.4 & \beta &= 45^\circ \\ \rho_\infty &= 8 \times 10^{17}\ \mathrm{kg/m^3} & A &= 1.0 \\ T_D &= 0\ \mathrm{K} & \varepsilon_{a,b} &= 0.80 \end{aligned}$$

The initial guess for each temperature was the free-stream value, $T_\infty = 200$ K. Despite jumping to nearly $11 T_\infty$ on the first iteration, the method quickly relaxed the temperatures down to their correct values after just ten DSMC steps. Indeed, this procedure is robust and stable as long as the initial guess for surface temperature is within roughly 2 orders of magnitude of the target value.

Note in the figure that the difference between T_a and T_b is a result of finite thermal conductivity through the panel. This DSMC simulation was repeated using all combinations of the following parameters,

$$\begin{aligned} M_\infty &= \{5, 10, 20, 30\} \\ \beta &= \{15^\circ, 45^\circ, 75^\circ\} \\ \kappa &= \{2, 20\}\ \mathrm{W/m^2K} \end{aligned}$$

Results of these DSMC simulations are plotted in Fig. 7 and compared to theory[9] using similarity parameters defined by

$$H_a = \sqrt{\frac{2}{\rho_\infty}}\left(\omega + \frac{\zeta_{int}}{2}\right)\left(\frac{\varepsilon_a \sigma}{\kappa}\right)^{1/3} \times A\left(n_\infty k T_\infty\right)^{3/2} Z \quad (14)$$

$$\eta_{a,b} = \left(\frac{\varepsilon_{a,b}\sigma}{\kappa}\right)^{1/3} T_{a,b} \quad (15)$$

where

$$\omega = 5/2 + S^2 - \left(\frac{\exp\left(-S^2 \sin^2\beta\right)}{4\sqrt{\pi} Z}\right) \quad (16)$$

$$Z = \frac{S \sin\beta}{2}\left[1 + \mathrm{erf}\left(S \sin\beta\right)\right] + \left(\frac{\exp\left(-S^2 \sin^2\beta\right)}{2\sqrt{\pi}}\right). \quad (17)$$

Again, DSMC results for T_a and T_b agree with theory over the entire flow range, validating the coupling of the DSMC method and the surface temperature model.

Heat Capacity and Dynamic Thermal Response

Non-zero material heat capacity leads to surface temperatures which will respond dynamically to a transient convective heating pulse, $q(t)$. Equations (2) were coupled into the DSMC technique to simulate free molecular flow of N_2 past a thin panel under the following conditions,

$$\begin{aligned} M_\infty &= 14 & \varepsilon_{a,b} &= 0.80 \\ \gamma &= 1.4 & \kappa &= 60\ \mathrm{W/m^2K} \\ \rho_\infty &= 5.00 \times 10^{-7}\ \mathrm{kg/m^3} & c_{a,b} &= 2000.0\ \mathrm{J/m^2K} \\ T_\infty &= 200\ \mathrm{K} & \tau &= 250\ \mathrm{s} \\ \beta &= 45^\circ & T_D &= 150\ \mathrm{K} \\ A &= 1.0 \end{aligned}$$

The form of the heating pulse was an empirical fit to an aerobraking profile[7] and is given by

$$q(t) = \frac{1}{2} Q\left(1 - \cos\frac{t}{\tau}\pi\right)\exp\left(-2 - 2\cos\frac{t}{\tau}\pi\right), \quad (18)$$

where τ represents a time constant such that peak heating occurs at $t = \tau$ and the duration of the entire heating pulse is 2τ. The initial surface temperatures, $T_a(0)$ and $T_b(0)$, are assumed to equal the deep-space temperature T_D.

The simulation predicted a peak heating value of Q = 11529.4 W/m^2 at perigee and a front-side perigee temperature of T_a = 370.8 K and a peak temperature of T_a = 460.5 K during the heating pulse. These points are plotted in Fig. 8 along with the temporal heating and temperature profiles obtained through numerical integration of Eqs. (2) for the same peak heating condition. The contribution from each mode of heat transfer is plotted. Note that the coupled DSMC temperature predictions compare well with the integrated results. These temporal profiles demonstrate that the non-zero heat capacity of the panel material caused the peak temperatures to occur after peak heating.

This simulation was repeated for $M_\infty = \{5, 10, 15, 30\}$ and the results were plotted in Fig. 9. DSMC surface temperatures compare well to analytic solutions from Eqs (2). Note from the analytic curves that, except at the highest and lowest energies, these temperatures are well below those corresponding to perfect insulators (κ=0) or perfect conductors (κ=∞) in radiative equilibrium. These results not only validate the DSMC implementation of the dynamic, coupled, model from Eqs. (2), but also demonstrate the significant differences between the various models.

Concluding Remarks

These results demonstrate that thermal conductivity and heat capacity play significant roles in establishing the surface temperatures of thin panels in rarefied hypersonic flow during dynamic aeropass maneuvers. DSMC simulations of flows past isothermal plates proved that under many conditions, particularly in highly-rarefied flows, surface temperature has great impact upon vehicle aerodynamics and heat transfer. It follows that accurate simulation of aerobraking scenarios requires accurate assessment of these surface temperatures. For dynamic heating pulses, this is afforded by time-integration of the surface heat transfer equations (2) and coupling of the surface temperatures back into the flow simulation. As such, surface temperatures are computed directly in the DSMC technique rather than relying upon isothermal estimates. These models may be employed in continuum methods for computational fluid mechanics as well, although the effects of surface temperature may be less significant in the continuum flow regime.

The differential equations could be simpified for materials with zero heat capacity, representing a double-sided panel with finite thermal conductivity from front to back. This coupled model was validated through comparison of simulated surface temperatures over a large range of flow conditions to free molecule theory under the same conditions. Likewise, the models may be simplified further for perfect conductors in radiative equilibrium. Again, comparisons with free molecule theory validated this model over a large range of flow conditions. Naturally, these DSMC models may be applied regardless of Kn_∞; free molecule flow was studied here for validation purposes due to the ready availability of the corresponding analytic solutions.

Acknowledgements

The author acknowledges and appreciates the support of NASA-Ames Research Center and the Numerical Aerodynamic Simulation for use of their facilities. This work was sponsored by NASA grant NCC2-582.

References

[1] LYONS, D.T, SJOGREN, W., JOHNSON, W.T.K., SCHMITT, D. AND MCRONALD, A., "Aerobraking Magellan", *AAS Paper No.* 91-420, Durango, Colorado, Aug., 1991.

[2] BIRD, G.A., *Molecular Gas Dynamics*, Clarendon Press, Oxford, 1976.

[3] BAGANOFF, D. AND MCDONALD, J.D., "A Collision-Selection Rule for a Particle Simulation Method Suited to Vector Computers," *Physics of Fluids A*, Vol. 2, No. 7, 1990, pp. 1248–1259.

[4] HAAS, B.L., "Particle Simulation of Satellite Aerobraking with Couple Surface Heat Transfer," presented at the *18th International Symposium on Rarefied Gas Dynamics*, Vancouver, B.C., July, 1992. To appear in published proceedings.

[5] MCDONALD, J.D., "A Computationally Effecient Particle Simulation Method Suited To Vector Computer Architectures," Ph.D. Thesis, Stanford University, 1989.

[6] HAYES, W.D. AND PROBSTEIN, R.F., *Hypersonic Flow Theory*, Academic Press, New York, 1959.

[7] HAAS, B.L., "Particle Simulation of Rarefied Aeropass Maneuvers of the Magellan Spacecraft," *AIAA Paper No. 92-2923*, Nashville, July 1992.

[8] CAREY, V.P., "Stochastic Modeling of Transition Regime Heat Transfer from a Cylinder in High Speed Gas Flow," *AIAA Paper No. 93-0726*, Reno, Jan. 1993.

[9] ABARBANEL, S., "Radiative Heat Transfer in Free-Molecule Flow," *Journal of Aerospace Science*, Vol. 28, No. 4, 1961, pp. 299–307.

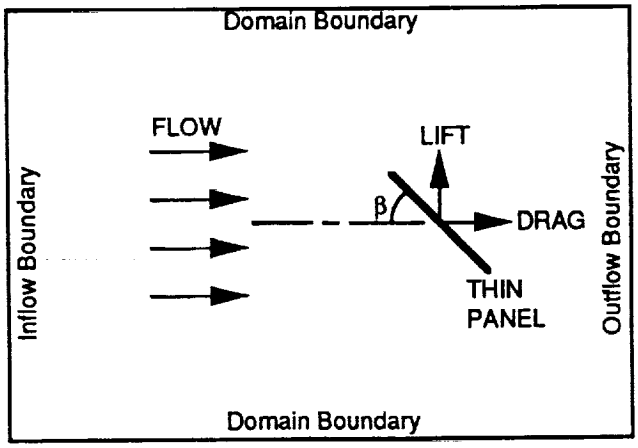

Fig. 1 Schematic representation of flow simulation geometry (not to scale).

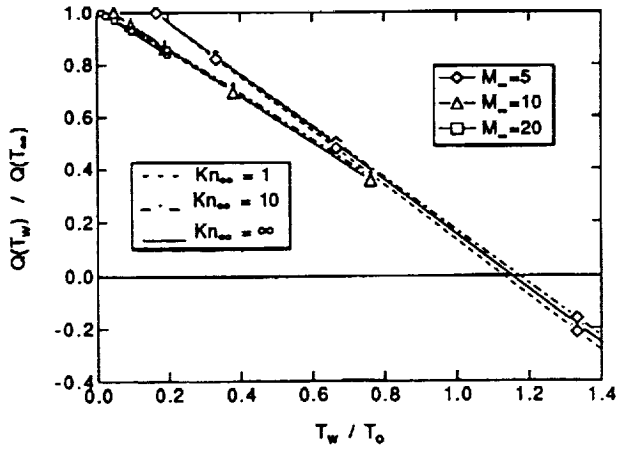

Fig. 2 Effects of T_w, M_∞, and Kn_∞ upon net convective heating q.

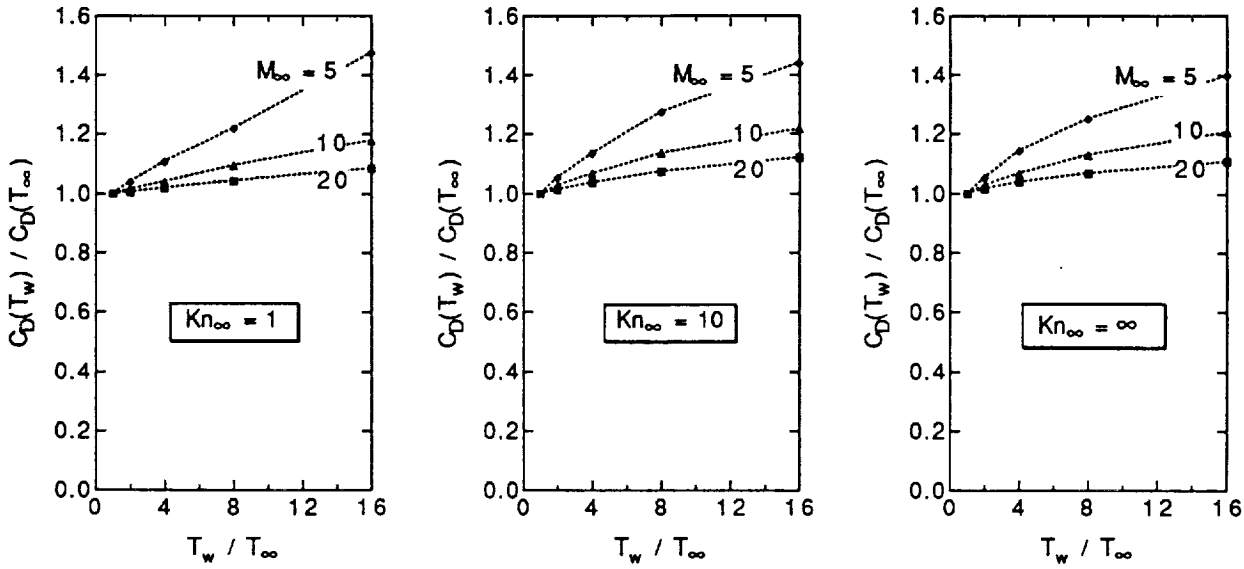

Fig. 3 Effects of T_w, M_∞, and Kn_∞ upon drag coefficient.

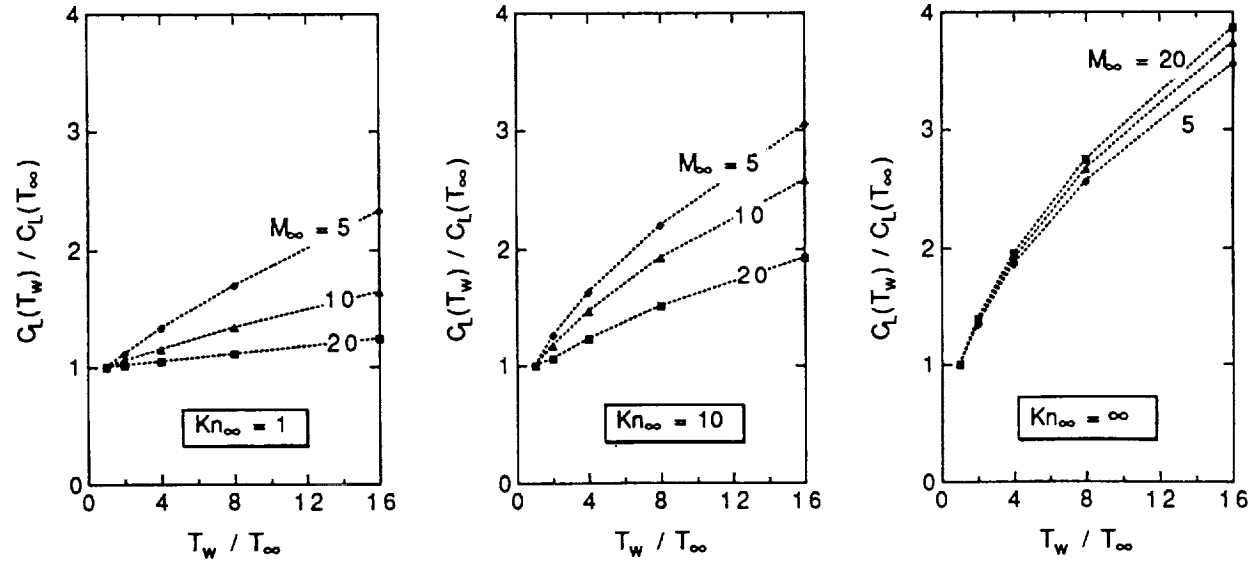

Fig. 4 Effects of T_w, M_∞, and Kn_∞ upon lift coefficient.

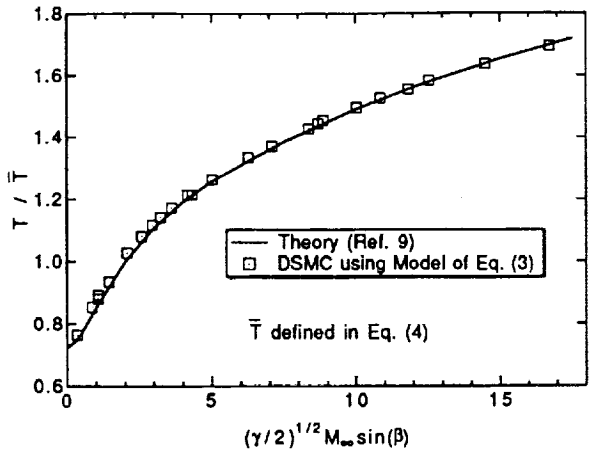

Fig. 5 Results from DSMC and theory for radiating, perfectly-conducting panels in free molecule flow.

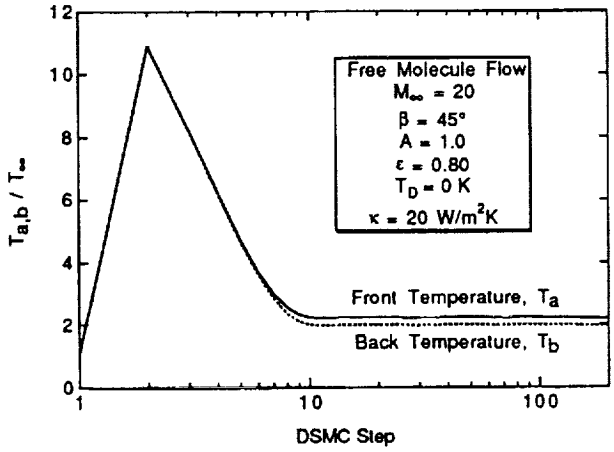

Fig. 6 Relaxation history for surface temperature computed in the DSMC code with the single-Newton-iteration scheme for radiating, conducting panels.

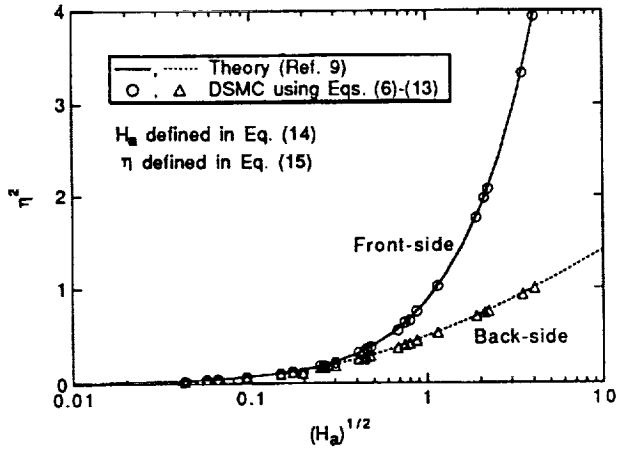

Fig. 7 Results from DSMC and theory for radiating, finitely-conducting panels in free molecule flow.

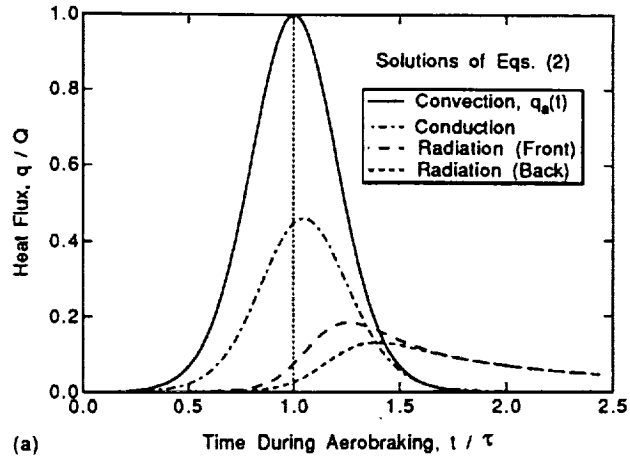

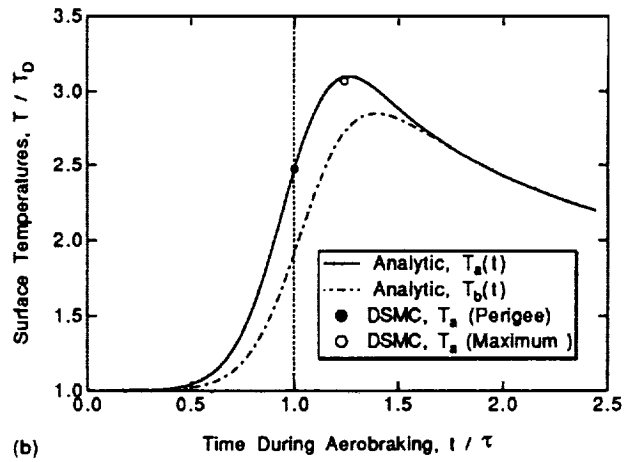

Fig. 8 Transient results from Eq. (2) for: (a) heating due to convection, conduction, and radiation; and (b) transient temperatures on each side of the panel. Temperatures are compared to DSMC results employing this model.

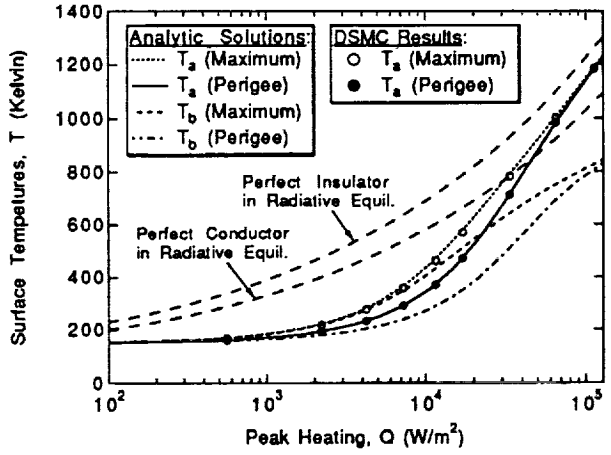

Fig. 9 Perigee and peak surface temperatures for front and back sides of a panel over a large range of peak convective heating. Solutions of Eq. (2) are compared to DSMC results using this model and to perfect conductors and insulators in radiative equilibrium.

Appendix C

AIAA 93-2806

Flow Resolution and Domain of Influence in Rarefied Hypersonic Blunt-body Flows

Brian L. Haas
Eloret Institute
Palo Alto, CA 94303

AIAA 28th Thermophysics Conference
July 6-9, 1993 / Orlando, FL

FLOW RESOLUTION AND DOMAIN OF INFLUENCE IN RAREFIED HYPERSONIC BLUNT-BODY FLOWS

Brian L. Haas*
Eloret Institute, Palo Alto, California 94303

This parametric study assesses the influence of upstream domain size and grid resolution upon flow properties and body aerodynamics computed for rarefied flows over cold blunt bodies with a direct simulation Monte Carlo (DSMC) particle method. Empirical correlations are suggested for aerodynamic coefficients for two-dimensional flows past a perpendicular flat plate. Free-stream parameters which were varied in the study include the Mach number, Knudsen number, surface temperature, and intermolecular potential. Insufficient grid resolution leads to overprediction of aerodynamic heating and forces in the DSMC method. Solution accuracy correlates well with the Reynolds number defined at the wall temperature and the stagnation mean free path relative to the cell dimension. Molecular diffusion from the body surface results in greater far-field domain influence as flow rarefaction increases. As a result, insufficient upstream domain size in the DSMC method leads to overprediction of heating and drag. Errors in aerodynamic coefficients correlate well with $\overline{x}$, the distance ahead of the body where flow temperature reaches half of its peak value. Engineering criteria for DSMC cell resolution and domain size are suggested. Simulation of a hard-sphere gas is more sensitive to grid resolution while simulation of a Maxwell gas is more sensitive to upstream domain size.

NOMENCLATURE

C	aerodynamic force coefficient
H	plate height
Kn	Knudsen number, λ/H
$\overline{\text{Kn}}$	Whitfield's correlation parameter, Eq. (6)
L	upstream domain size
$\overline{L}$	domain size correlation parameter, Eq. (18)
M	Mach number
Nu_w	Nusselt number at the wall, Eq. (7)
n	gas number density
Pr	Prandtl number, Eq. (8)
Q	free-stream kinetic heat flux, $\rho_\infty u_\infty^3/2$
q	aerodynamic net heat flux
Re	Reynolds number, Eqs. (2) and (3)
St	Stanton number, Eq. (9)
T	temperature
u	flow velocity
x	location relative to stagnation point
$\overline{x}$	distance from plate to T half-rise location
α	intermolecular potential exponent
γ	ratio of specific heats = 1.4
δ	length of a cubic grid cell
λ	gas mean free path
ρ	gas mass density

Superscripts:

*	presumed-correct value
DOM	pertains to domain effects
RES	pertains to resolution effects

Subscripts:

a	adiabatic wall condition
D	drag
ERR	error coefficient
L	lift over top half of body
s	stagnation value
w	wall value
∞	freestream value

INTRODUCTION

Flow field characteristics about blunt bodies during atmospheric entry lead to considerable challenges for computational simulation. Highly rarefied flows, where the gas density n is low and the mean free path λ between molecular collisions is high, are better suited to particle simulation methods, such as the direct simulation Monte Carlo (DSMC) technique pioneered by Bird,[1] rather than continuum techniques based upon the Navier-Stokes equations. DSMC methods employ many model particles whose motion and interaction simulate gas dynamics directly. The simulated flowfield is divided into a network of small cells to facilitate collision modeling and statistical sampling.

The computational burden of DSMC methods, however, grows proportionally with local gas density and the size of the computational domain. In typical entry flows, the body surface temperature is rather low compared with the stagnation temperature, leading to a steep density gradient near the body surface. Accurate simulation of this flow requires sufficient grid resolution near the body. Alternatively, the extent of freestream rarefaction results in a leading shock layer which is fully merged with the boundary layer of the body, yet extends far upstream. Accurate simulation therefore requires a large upstream computational

* Research Scientist. Member, AIAA.
Mailing Address: NASA Ames Research Center
M/S 230-2, Moffett Field, California 94035-1000

flow domain. Together, these requirements rapidly drive the computational cost of the particle simulation method upward. Hermina[2] and Woronowicz[3] studied grid resolution effects for flows over slender bodies and flat plates parallel to the free-stream direction. In contrast, the present study addresses flow over blunt bodies. Also, errors resulting from limited domain size became evident in recent computations of aerobraking of the Magellan spacecraft[4]. The DSMC researcher must therefore understand what simulation costs are necessary to obtain a solution of sufficient accuracy.

The objective of the present parameteric study is to assess quantitatively the sensitivity of aerodynamic loads and gas properties to grid resolution and simulation domain size in blunt-body, hypersonic, rarefied flows. In addition, correlations are suggested for aerodynamic coefficients and flow properties over a wide range of free-stream conditions.

METHODS OF ANALYSIS

The present study employed an efficient particle simulation technique[5,6] to investigate the net heat flux q and aerodynamic forces on a two-dimensional flat plate of height H facing perpendicular to the flow direction. Gas temperature T and number density n were also computed along the stagnation streamline. The following range of flow conditions were used:

$$\begin{aligned} M_\infty &= \{5, 10, 20\} \\ Kn_\infty &= \{0.1, 0.3, 1, 3, 10\} \\ T_w/T_\infty &= \{1, 5, 9\} \\ \alpha &= \{4, 8, \infty\}. \end{aligned}$$

For each flow case, the gas was modeled with two fixed internal degrees of freedom leading to a constant ratio of specific heats of $\gamma = 1.4$. Interaction of the gas with the plate surface at wall temperature T_w was modeled as fully diffuse and thermally accommodated. All simulations employed between 4 and 64 particles per cell as the input freestream number density, n_∞. The code used cubic cartesian cells of uniform dimension throughout the flowfield, but this does not alter the conclusions of the present work when applied to DSMC codes with variable cell dimensions.

For each set of flow conditions, the simulation resolution and domain were varied considerably and their effects upon solution accuracy were determined. Grid resolution is defined by the plate height H while the flow domain size is defined by the distance L of the computational field upstream of the plate, where both H and L are measured in units of grid cells of linear dimension δ. These length scales are depicted schematically in Fig. 1 along with $\bar{x}$ which represents the location, far upstream of the plate, where the local translational temperature first reaches half of its peak value.

Estimate of Local Mean Free Path

In the DSMC technique, two particles in the flow may collide only if they both reside in the same grid cell. Furthermore, any two particles within a given cell can collide regardless of their respective positions in the cell. The collision probability for a particular pair of neighboring particles is assessed as a function of molecular constants and the relative translational energy of the pair.[5] If the cell dimension δ near the cold body surface is too large, then energetic particles at the far edge of the cell are able to readily transmit momentum and energy to particles immediately adjacent to the surface. The latter particles may, in turn, transmit that energy and momentum to the surface. This leads to overprediction of both the surface heat flux and the aerodynamic force on the body than would occur in the real gas. This error is minimized by reducing the cell dimension relative to the local mean free path of molecules near the surface. From equilibrium kinetic theory, where translational velocities have a Maxwellian distribution, the local mean free path λ is related to the local number density n and temperature T as follows,

$$\frac{\lambda}{\lambda_\infty} = \left(\frac{n_\infty}{n}\right)\left(\frac{T}{T_\infty}\right)^{2/\alpha}. \qquad (1)$$

The exponent of the assumed inverse-power intermolecular potential, α, may vary between the limits of the Maxwell molecule ($\alpha = 4$) and the hard sphere ($\alpha = \infty$). The expression in Eq. (1) is not exact for flows far from translational equilibrium, but will suffice to characterize the degree of rarefaction in the flow. Employing the stagnation temperature and density near the plate surface from the DSMC simulation leads to an approximation of the stagnation mean free path, λ_s. Theoretical estimates of λ_s were derived by Whitfield,[7] but were limited to particular flow conditions and were not as convenient as the simple expression in Eq. (1) for use in the present study.

As a consequence of Eq. (1), regions of high density lead to short mean free paths, requiring finer cell resolution to capture flow gradients accurately. Such behavior characterizes hypersonic rarefied flows near cold blunt-body surfaces.

FLOW CHARACTERISTICS AND CORRELATIONS

Having computed flow properties and aerodynamics over a wide range of input conditions and simulation parameters, it proved instructive to summarize the most accurate results; that is, those corresponding to grids of sufficient resolution and domains of sufficient size.

Flow Along the Stagnation Streamline

Density profiles along the stagnation streamline upstream of the plate are plotted in Fig. 2a to demonstrate the effects of free-stream rarefaction. Note that the density at the plate surface (at $x/H = 0$) is significantly higher than the free-stream value. This behavior is slightly more pronounced, and the gradients are steeper, for flows at lower Kn_∞. This, combined with the fact that lower Kn_∞ means that the freestream λ_∞ is short, dictates that the cell resolution must be very fine compared with more rarefied

flows. Notice that there is no real shock structure ahead of the body except at the lowest Kn_∞.

Temperature profiles along the stagnation streamline for these same flows are plotted in Fig. 2b. Temperature was defined by the variance of particle velocities. These curves clearly demonstrate that the body influences the flow far upstream. This domain of influence increases with Kn_∞ as a result of upstream diffusion of particles which reflected from the body surface. By contrast, Kn_∞ has little effect upon the resultant stagnation temperature and density at the plate surface.

For a given free-stream Knudsen number, the effects of Mach number on the streamline profiles is demonstrated in Fig. 3. Greater Mach number leads to significantly greater stagnation density and temperature, as well as greater peak temperature. However, unlike Kn_∞, M_∞ has very little effect on the extent of the domain of influence upstream of the plate.

As is evident in the profiles in Fig. 4, however, wall temperature T_w affects all flow properties including the peak temperatures, stagnation values, and the extent of the domain of influence of plate in these rarefied flows. This results from particles reflecting from hotter surfaces with greater energies, leading to greater relative translational velocities and flow temperatures. Energetic reflections from the hotter surface reduces the net buildup of particle density near the plate.

Finally, the effects of employing different exponents α of the intermolecular potential are demonstrated in Fig. 5. Just as with Kn_∞, different potentials have little effect upon the stagnation temperature or density, but lower values of α greatly increase the extent of the domain of influence upstream of the body. Plotting the local mean free path as computed with Eq. (1) shows that λ is much greater for $\alpha = 4$ than for $\alpha = \infty$. The flow therefore becomes effectively more rarefied, and the profiles are indicative of those corresponding to large Kn_∞ in Fig. 2. Also, the gradients for the hard-sphere are steeper and lead to lower λ_s at the stagnation point on the body compared to the Maxwell-molecule. As a consequence, accurate DSMC solutions for hard-sphere gases require finer cell resolution while solutions for Maxwell-molecule gases require larger upstream computational fields.

Many of these effects are summarized by plotting λ_s and $\bar{x}$ for all flow conditions. The stagnation mean free path correlated fairly well with the product $Re_w Kn_\infty^{3/4}$ as plotted in Fig. 6. The Reynolds number based on the wall temperature is defined from the temperature dependence of the coefficient of viscosity and is given by

$$Re_w = Re_\infty \left(\frac{T_\infty}{T_w}\right)^{1/2-2/\alpha}, \tag{2}$$

where the free-stream Reynolds number is determined from Bird's definition of mean free path[8] as follows,

$$Re_\infty = \frac{2}{15}(6-4/\alpha)(4-4/\alpha)\left(\frac{\gamma}{2\pi}\right)^{1/2}\frac{M_\infty}{Kn_\infty}. \tag{3}$$

This correlation takes into account the effects of all flow parameters (M_∞, Kn_∞, α, and T_w) and demonstrates that λ_s is strongly dependent upon M_∞ and weakly upon Kn_∞. Employing a least-squares log-log fit to the data in Fig. 6 leads to the following simple expression for the stagnation mean free path for these flows,

$$\lambda_s = \frac{\lambda_\infty}{2\,Re_w\,Kn_\infty^{3/4}}. \tag{4}$$

As plotted in Fig. 7, the upstream extent $\bar{x}$ of the domain of influence of the body is correlated against the product,

$$\left(\frac{1}{1-2/\alpha}\right)\left(\frac{T_\infty}{T_w}\right)^{1/4}\frac{Kn_\infty}{Re_w}. \tag{5}$$

Again, this gives a fair correlation and encompasses all parameters. Here, $\bar{x}$ exhibits strong dependence upon Kn_∞ than upon M_∞.

All correlations suggested in the present study were developed through parameterization. That is, simulation results for cases with identical flow conditions except for a given parameter were compared with each other to assess dependence upon the given parameter. Simulation results were plotted using quantities multiplied by powers of the independent parameters.

Correlations for Aerodynamic Coefficients

No existing theory describes completely the heating and aerodynamic loading of bodies over the entire range of Reynolds number. The objective here is only to estimate the dependencies of the aerodynamic coefficients upon flow conditions empirically, rather than develop a detailed theory for them. In addition to numerous experimental investigations, previous computational attempts to identify correlation parameters have met with some success, including those of Woronowicz[9] for flat plates parallel to the free-stream flow, and Gilmore and Harvey[10] for flat-ended cylinders. The latter work concludes that Whitfield's parameter $\overline{Kn}$, defined by

$$\overline{Kn} = Kn_\infty\left(\sqrt{\gamma\frac{\pi}{2}\frac{T_\infty}{T_w}}\,M_\infty + 1\right)^{-1}, \tag{6}$$

is reasonable for correlating heat transfer. The results of the present study employed this parameter to correlate the wall Nusselt number, Nu_w, divided by $\sqrt{Kn_\infty}$, to obtain the result plotted in Fig. 8. Here, Nu_w is defined from the following expressions

$$Nu_w = Re_w\,Pr\,St \tag{7}$$

$$Pr = \frac{4\gamma}{9\gamma-5} \tag{8}$$

$$St = \frac{\gamma-1}{2}M_\infty^2\,\frac{q/Q}{\frac{T_a}{T_\infty}-\frac{T_w}{T_\infty}} \tag{9}$$

$$\frac{T_a}{T_\infty} \approx 2\frac{\gamma-1}{\gamma+1}\left(\frac{\gamma}{\gamma-1}+\frac{\gamma}{2}M_\infty^2\right). \tag{10}$$

The last expression closely approximates the adiabatic wall temperature for free molecule flows[11] and is assumed to be a fair estimate for the rarefied flows studied here.

Aerodynamic drag and lift on the plate did not vary significantly among the flow cases, but did exhibit some weak correlation to the ratio Re_w/Kn_∞ as plotted in Fig. 9. In the present context, the lift coefficient C_L is defined by the body force, perpendicular to the flow direction, over the top half of the plate only. Defining C_L in this way yields a parameter which will prove below to be sensitive to grid resolution and domain size. Naturally, integrating the force over the top and bottom halves of the plate would yield zero lift force due to symmetry.

GRID RESOLUTION

For all flow conditions within the Knudsen number range, $0.1 \leq Kn_\infty \leq 1.0$, simulations were performed to assess the effects of grid resolution upon solution accuracy. Since all flow parameters and aerodynamic coefficients are normalized by the plate height, grid resolution was defined by the ratio H/δ. At each flow condition, simulations were performed using plates measuring $H/\delta = \{2, 4, 6, 10, 20, 40, 60, 100, 200, 400\}$.

Resolution Effects On Flow Profiles

The density and temperature profiles along the stagnation streamline ahead of the body are plotted in Fig. 10. For the coarse grids, where $H/\delta<100$, the profiles were smeared considerably. For $H/\delta\geq100$, the profiles coalesced to a single form and were assumed therefore to represent accurate solutions. This same general behavior was observed for all flow conditions, although the resolution required to capture the appropriate profiles did not need to be as fine at larger Kn_∞ compared with lower Kn_∞. For example, at $Kn_\infty=1.0$, accurate profiles were obtained at $H/\delta\geq60$.

Resolution Effects On Aerodynamic Coefficients

For each simulation, the coefficients for heating and aerodynamic forces were computed. To assess the errors corresponding to a given flow resolution, the aerodynamic coefficients computed with the finest resolution at each flow condition were assumed to represent the "correct" values for that flow. It was the stagnation density and temperature from that solution which was also used to determine λ_s as plotted in Fig. 6.

As observed qualitatively for all flow conditions, coarse grid resolution led to overprediction of heating, drag, and lift. The errors dropped considerably with finer resolution. Errors in the aerodynamic coefficients were correlated and plotted against the product $\lambda_s Re_w/\delta$ in Fig. 11. Best agreement was obtained, through parameterization, by employing error coefficients defined as follows,

$$(q)_{ERR}^{RES} = 10^{4/\alpha} \left(\frac{Kn_\infty}{Re_w}\right)^{1/2} \left(\frac{q}{q^*} - 1\right) \quad (11)$$

$$(C_D)_{ERR}^{RES} = 5^{4/\alpha} \left(\frac{C_D}{C_D^*} - 1\right) \quad (12)$$

$$(C_L)_{ERR}^{RES} = Re_w^{-1/2} \left(\frac{C_L}{C_L^*} - 1\right). \quad (13)$$

Superscript "$*$" denotes the value for the coefficient which was assumed to be most accurate from the finest resolution simulation. These plots provide an engineering assessment of the accuracy associated with a given grid resolution, in terms of stagnation mean free path, for a given set of flow conditions. Scatter in the plots resulted from imperfect correlation parameters and the statistical limitations inherent to the DSMC technique. Scatter is particularly noticeable at the highest resolutions where the errors are small relative to the accuracy of the simulation method.

A suitable criterion for engineering applications, which estimates that the error coefficients will drop by two orders of magnitude, specifies a cell resolution near the body surface dictated by the stagnation mean free path as follows,

$$\delta \leq \lambda_s \frac{Re_w}{20}. \quad \text{Resolution Criterion} \quad (14)$$

Employing the linear fit from Eq. (4) leads to the criterion in terms of flow input parameters only,

$$\delta \leq \frac{\lambda_\infty}{40\, Kn_\infty^{3/4}}. \quad \text{Resolution Criterion} \quad (15)$$

DOMAIN SIZE

For rarefied flows in the higher Knudsen number range ($1.0\leq Kn_\infty \leq 10.0$), simulations were performed to assess the influence of the upstream flow field domain upon solution accuracy. In view of the results above, the cell resolution used in each case here was sufficiently fine such that the stagnation mean free path exceeded one cell-length near the body. The objective here was to employ different upstream computational field sizes, defined by length L in Fig. 1, to determine the minimum acceptable domain size required for a given penalty in solution accuracy. At each flow condition, simulations were performed using domains of dimensions $L/H = \{0.1, 0.2, 0.5, 1, 2, 4, 8, 16, 32\}$.

Domain Size Effects On Flow Profiles

Flow density and temperature along the stagnation streamline are plotted for one flow condition in Fig. 12 employing different domain sizes L. With sufficiently large L, all the curves coalesced to a single curve to represent the assumed correct profile as represented at $L/H = 32$. With insufficient upstream domain (i.e. small L), density and upstream temperature are underpredicted while the peak temperature is overpredicted. However, once the simulation

domain size exceeded roughly twice the distance of the temperature half-rise point, $\overline{x}$, the temperature and density profiles followed the expected forms predicted when ample upstream domain was employed. Although not presented here, behavior for all other flow conditions are qualitatively similar to these results.

Domain Size Effects On Aerodynamic Coefficients

Quantitative assessment of the errors in aerodynamic loads on the plate for simulations employing different upstream domain sizes are presented in Fig. 13. The errors for each case are computed relative to the aerodyanmic loads which were obtained using the largest domain L and presumably represent the correct values. Each plot employs a length scale normalized by $\overline{x}$. As expected, the errors in predicted aerodynamics decreased as larger upstream domain sizes were used. Aerodynamic heating q and drag C_D were overpredicted in all cases. The lift forces were so small for these rarefied flows that the errors for each domain size were negligible relative to the statistical fluctuation of the simulation, and were therefore not plotted. Through parameterization, the best correlations over the range of flow conditions employed error coefficients defined by,

$$(q)_{ERR}^{DOM} = \left(\frac{1+4/\alpha}{1-2/\alpha}\right) \mathrm{Kn}_\infty^{3/2} \left(\frac{T_\infty}{T_w}\right)^{1/8} \left(\frac{q}{q^*} - 1\right) \quad (16)$$

$$(C_D)_{ERR}^{DOM} = \left(\frac{1+4/\alpha}{1-2/\alpha}\right) \mathrm{Kn}_\infty^{3/2} \left(\frac{T_\infty}{T_w}\right)^{1/8} \left(\frac{C_D}{C_D^*} - 1\right) \quad (17)$$

and a domain-size correlation-parameter given by

$$\overline{L} = \frac{L}{\overline{x}} \left(\frac{T_\infty}{T_w}\right)^{1/8} \left(\frac{1}{1+2/\alpha}\right). \quad (18)$$

Note that the data levels off as the domain size parameter $\overline{L}$ drops below roughly 0.3. In the limit of decreasing upstream domain, the incoming flow is almost completely unaffected by particles reflecting from the plate surface such that the aerodynamic loads approach the values corresponding to the free molecular flow limit. For heating and drag, the limit is less erroneous for flows at greater freestream Knudsen numbers Kn_∞ since free molecular flow represents the limit of greatest possible rarefaction. The interesting paradox is that, while the domain of upstream influence increases with Kn_∞, the penalty in terms of solution accuracy is less dramatic compared to simulations at lower Kn_∞.

For engineering purposes, an appropriate criterion for defining a suitable computational flow domain for rarefied flow simulation is given when the error coefficients drop by two orders of magnitude, leading to the criterion,

$$\overline{L} \geq 2. \quad \text{Domain Criterion} \quad (19)$$

CONCLUDING REMARKS

When employing direct particle simulation methods, accurate simulation of highly rarefied flows about cold blunt bodies requires sufficient computational grid resolution and upstream flow domain size. The objective of this parametric study was to assess quantitatively what penalty is suffered in solution accuracy when minimizing computational expense by using short domains and coarse grids. Qualitative results were similar for all free-stream conditions. Criteria for grid resolution and domain size were expressed in terms of flow properties λ_s and $\overline{x}$. These criteria apply specifically to the two-dimensional flow about a flat plate perpendicular to the freestream direction when $\gamma = 1.4$. However, these results likely apply to any cold-wall, blunt-body, hypersonic, rarefied flow problem. Empirical correlations were suggested for stagnation streamline properties and aerodynamic loading over the range of flow conditions.

ACKNOWLEDGEMENTS

The author would like to thank Dr. Wahid Hermina (Sandia National Laboratory) and Michael Fallavollita (Stanford University) for helpful dicussions which led to this parametric study. The author acknowledges and appreciates the support of NASA-Ames Research Center and the Numerical Aerodynamic Simulation for use of their facilities. This work is sponsored by NASA grant NCC2-582.

REFERENCES

[1] BIRD, G.A., *Molecular Gas Dynamics*, Clarendon Press, Oxford, 1976.

[2] HERMINA, W.L., "Monte Carlo Simulation of Rarefied Flow Along a Flat Plate," *AIAA Paper No. 87-1547*, June 1987.

[3] WORONOWICZ, M.S., "Application of a Vectorized Particle Simulation To The Study of Plates and Wedges in High-Speed Rarefied Flow," Ph.D. Thesis, Dept. of Aeronautics and Astronautics, Stanford University, 1991.

[4] HAAS, B. L., "Particle Simulation of Rarefied Aeropass Maneuvers of the Magellan Spacecraft," *Journal of Spacecraft and Rockets*, to be published, 1993. Revision of AIAA Paper No. 92-2923.

[5] BAGANOFF, D. AND MCDONALD, J.D., "A Collision-Selection Rule for a Particle Simulation Method Suited to Vector Computers," *Physics of Fluids A*, Vol. 2, No. 7, 1990, pp. 1248–1259.

[6] MCDONALD, J.D., "A Computationally-Efficient Particle Simulation Method Suited to Vector Computer Architectures," Ph.D. Thesis, Dept. of Aeronautics and Astronautics, Stanford University, 1989.

[7] WHITFIELD, D.L., "Mean Free Path of Emitted Molecules and Correlation of Sphere Drag Data," *AIAA Journal*, Vol. 11, No. 12, 1973, pp. 1666–1670.

[8] BIRD, G.A., "Definition of Mean Free Path for Real Gases," *Physics of Fluids*, Vol. 26, No. 11, 1983, pp. 3222–3223.

[9] WORONOWICZ, M.S. AND BAGANOFF, D., "Drag and Heat Transfer Correlations for Rarefied Flow Past Flat Plates," *Journal of Thermophysics and Heat Transfer*, Vol. 7, No. 1, 1993, pp. 63–67.

[10] GILMORE, M.R. AND HARVEY, J.H., "Effects of Mach Number, T_{wall}, T_∞, and Thermal Accommodation Coefficient On Flow Around Bluff Bodies in the Rarefied Regime." Presented at the 18th Symposium on Rarefied Gas Dynamics, Vancouver, BC, Canada, July, 1992. To appear in published proceedings.

[11] OPPENDHEIM, A.K., "Generalized Theory of Convective Heat Transfer in a Free-Molecule Flow," *Journal of the Aeronautical Sciences*, Vol. 20, No. 1, 1953, pp. 49–58.

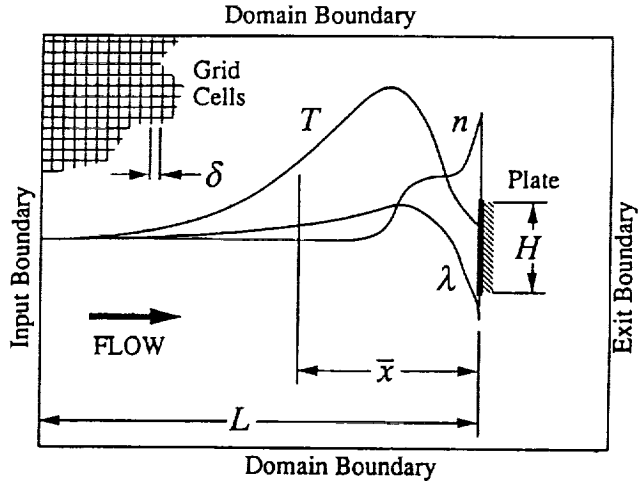

Fig. 1 Definition of simulation length-scales and schematic representation of temperature and density profiles upstream of a cold plate of dimension H in rarefied flow.

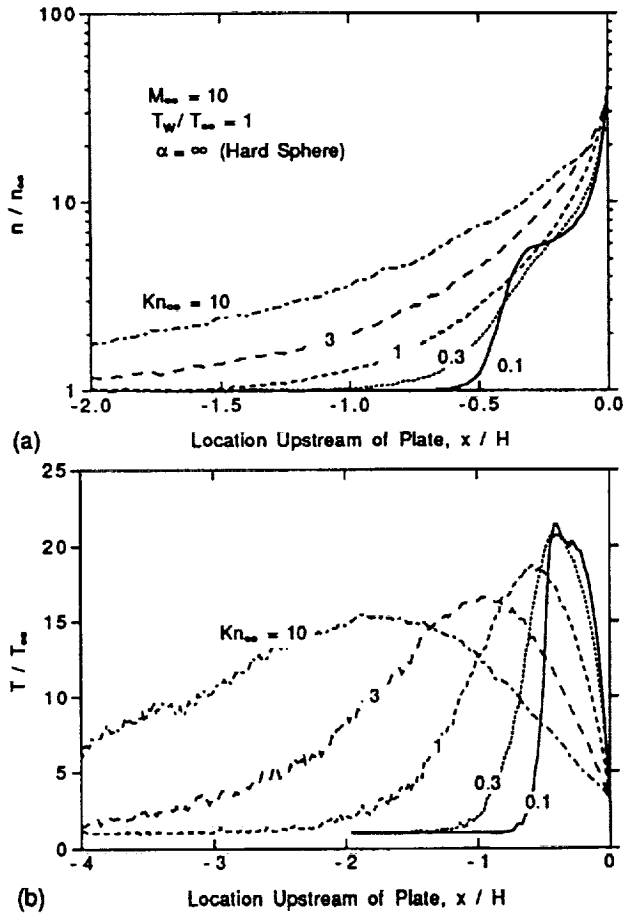

Fig. 2 Effects of flow rarefaction, Kn_∞, upon profiles along the stagnation streamline; (a) number density, n; (b) temperature, T.

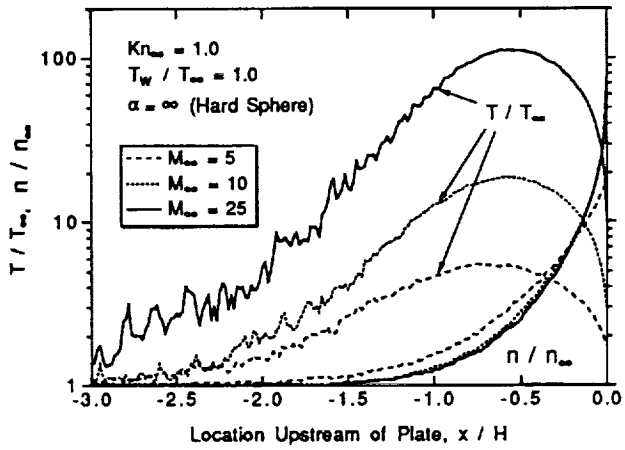

Fig. 3 Effects of Mach number, M_∞, upon profiles along the stagnation streamline.

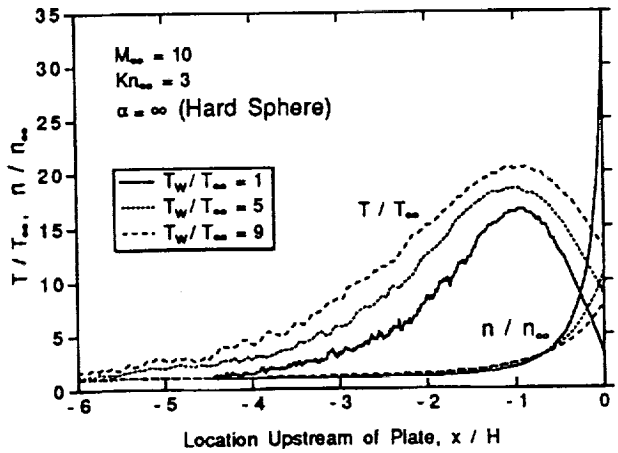

Fig. 4 Effects of wall temperature, T_w, upon profiles along the stagnation streamline.

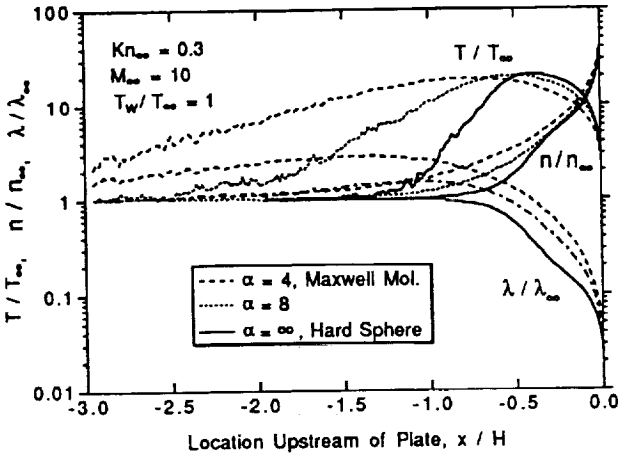

Fig. 5 Effects of intermolecular potential, α, upon profiles along the stagnation streamline.

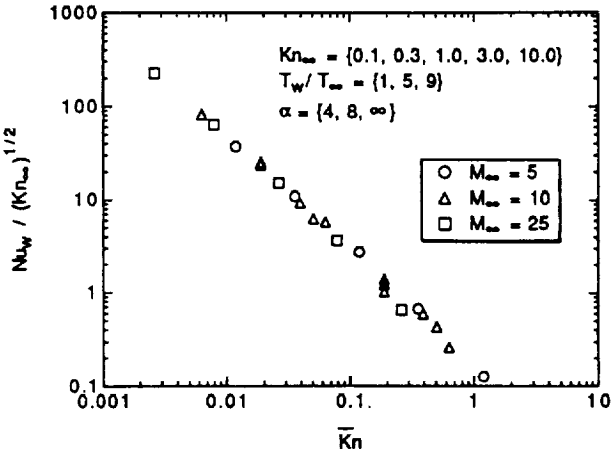

Fig. 8 Empirical correlation for plate heating.

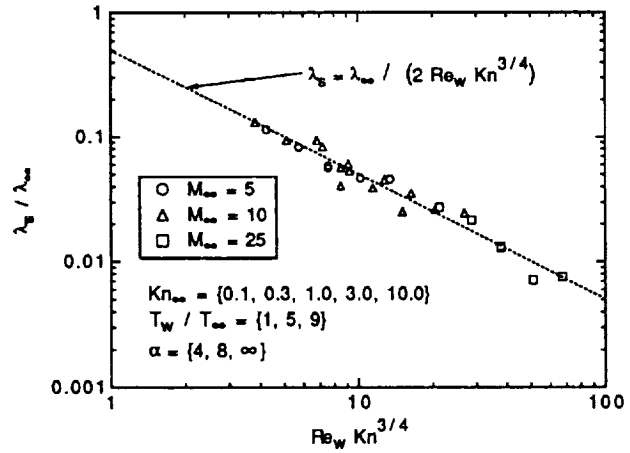

Fig. 6 Empirical correlation for the stagnation mean free path.

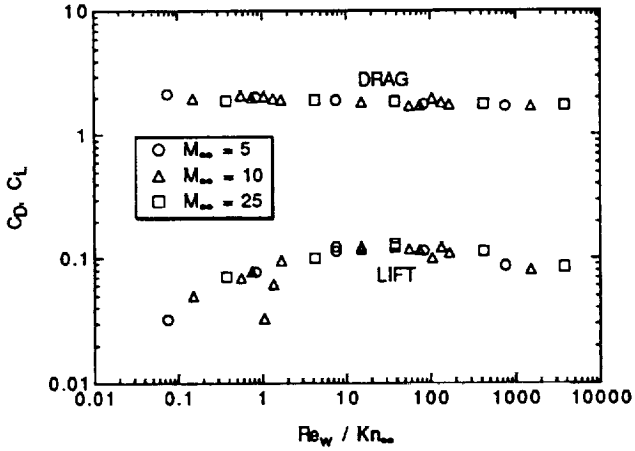

Fig. 9 Empirical correlation for plate drag and lift forces.

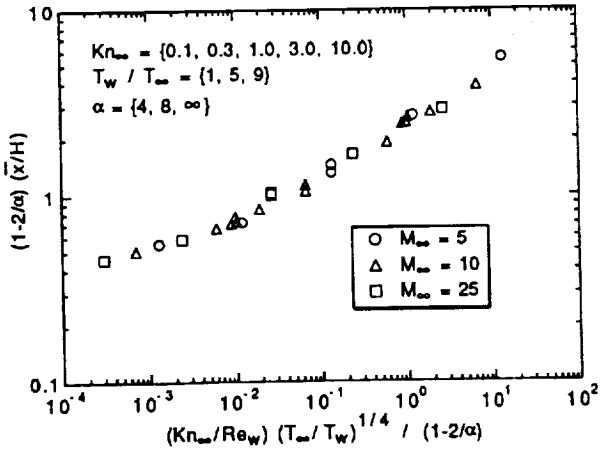

Fig. 7 Empirical correlation for the extent of the domain of influence upstream of the body.

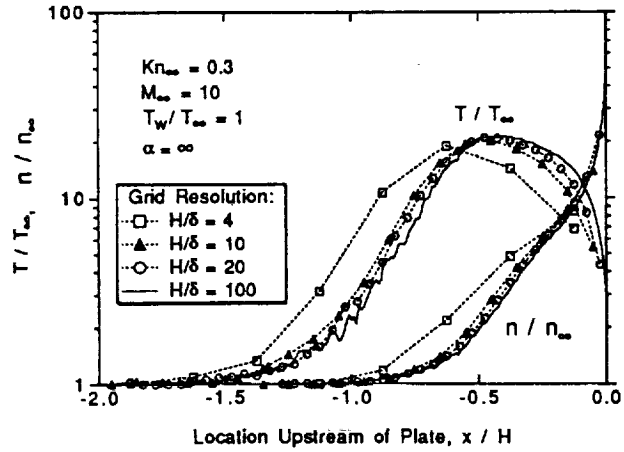

Fig. 10 Effect of grid resolution upon profiles along the stagnation streamline upstream of the plate.

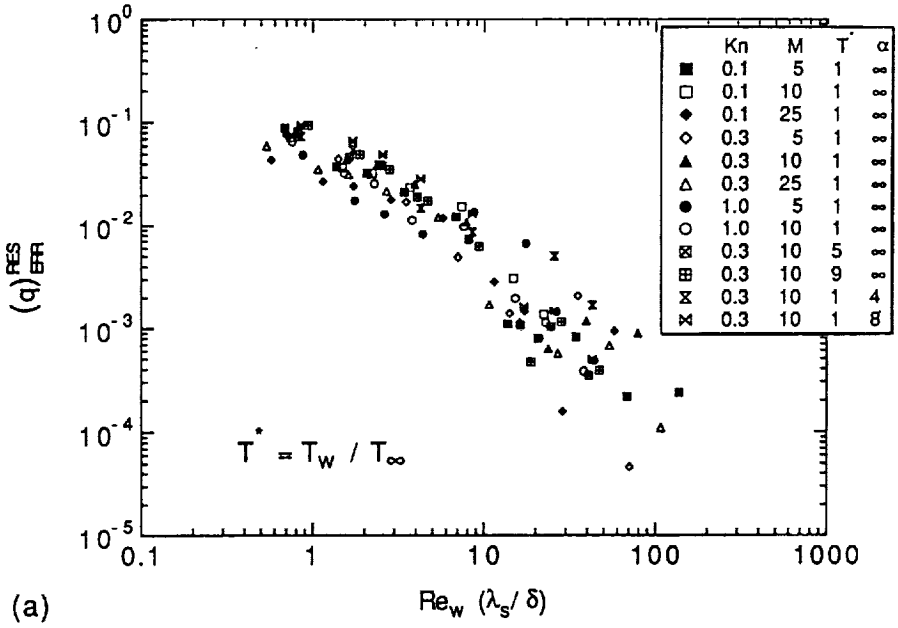

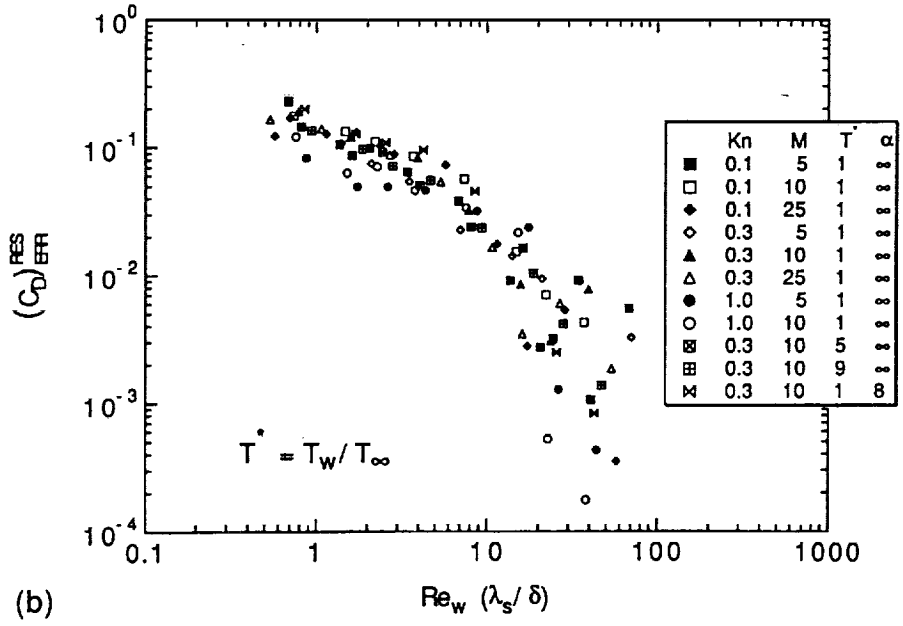

Fig. 11 Correlated effect of DSMC grid resolution upon aerodynamic coefficients for all flow conditions; (a) heating; (b) drag; (c) lift.

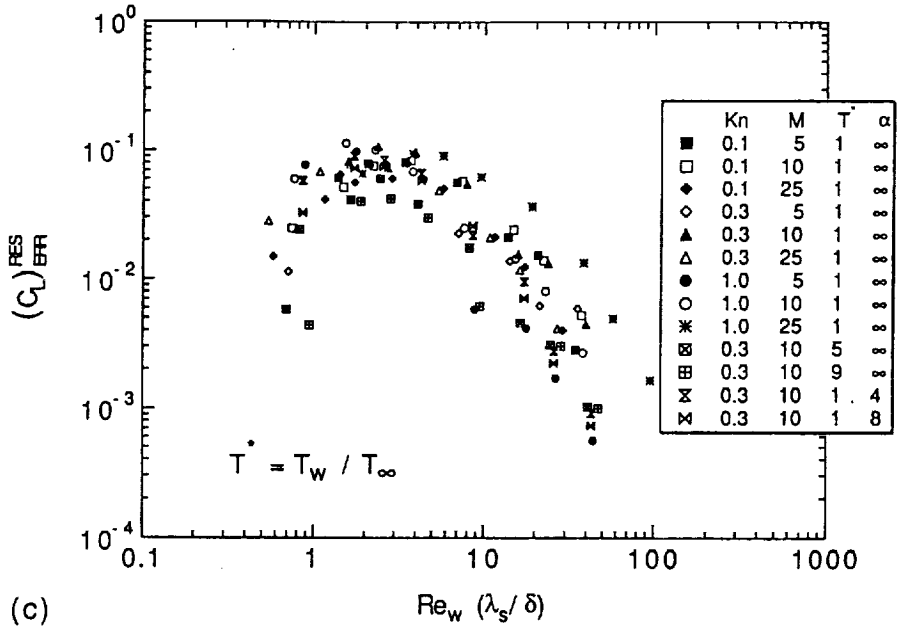

Fig. 11 (continued)

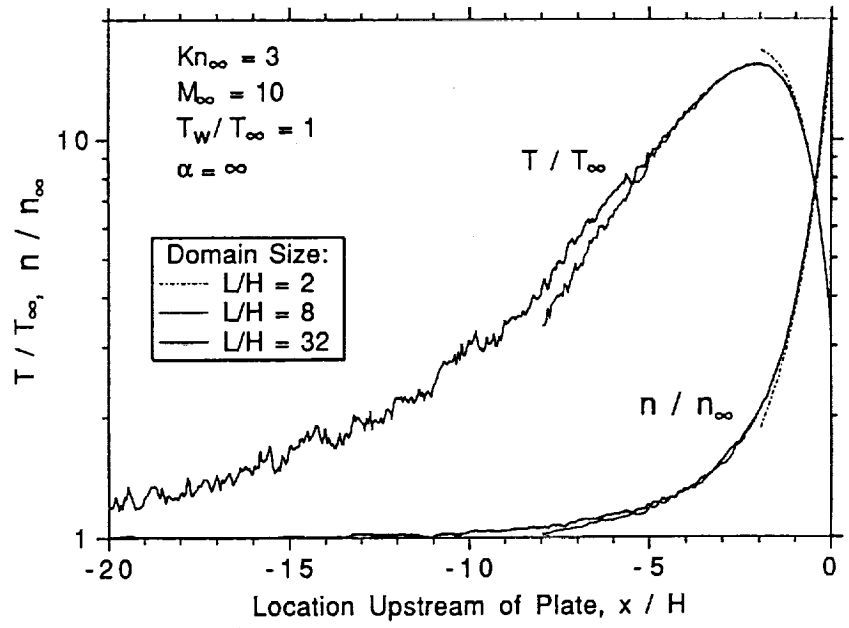

Fig. 12 Effect of DSMC domain size upon profiles along the stagnation streamline upstream of the plate.

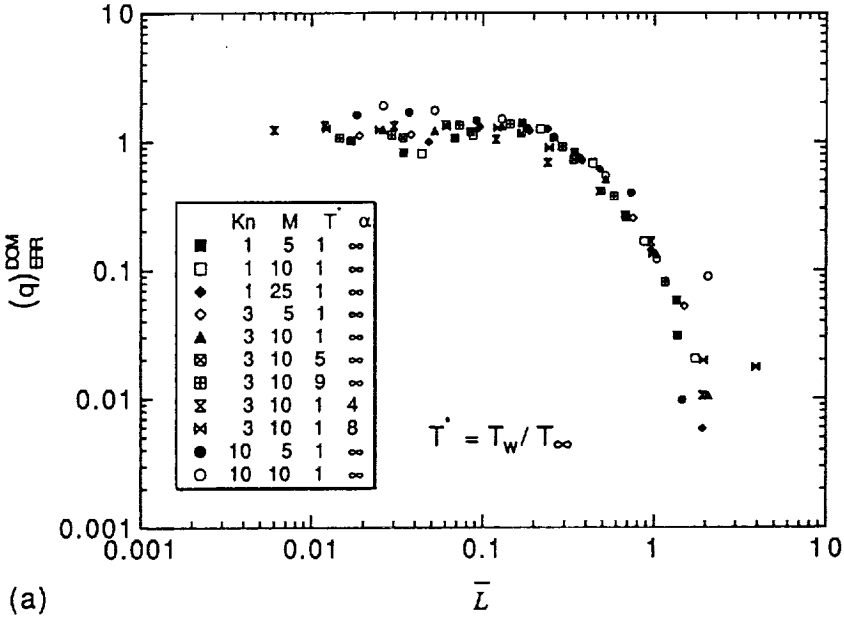

(a)

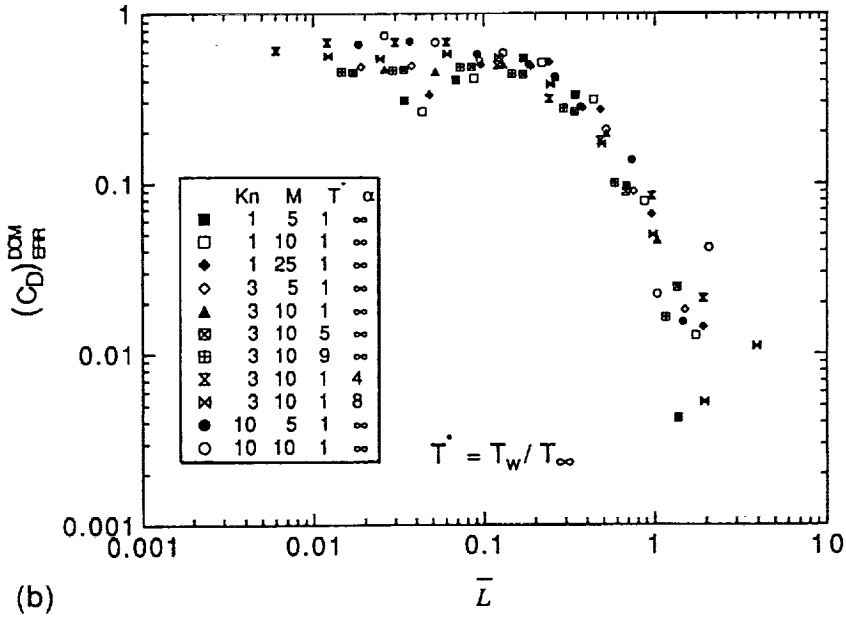

(b)

Fig. 13 Correlated effect of DSMC domain size upon aerodynamic coefficients for all flow conditions; (a) heating; (b) drag.

Appendix D

SIMULATED RAREFIED AERODYNAMICS OF THE MAGELLAN SPACECRAFT DURING AEROBRAKING

Brian L. Haas*
Eloret Institute, Palo Alto, California 94303

Durwin A. Schmitt†
Martin Marietta Astronautics Company, Denver, Colorado

Aerodynamic loads upon the Magellan spacecraft during aerobraking through the atmosphere of Venus are computed at off-design attitudes with a direct simulation Monte Carlo (DSMC) particle method. This method is not restricted to the assumption of collisionless flow normally employed to assess spacecraft aerodynamics. Simulated rarefied flows at nominal altitudes near 140 km and an entry speed of 8.6 km/s were compared to simulated and analytic free molecular results. Aerodynamic moments, forces, and heating for rarefied entry at all attitudes were 7– 10% below free molecular results. All moments acted to restore the vehicle to its nominal zero-pitch, zero-yaw attitude. Suggested canting of the solar panels is an innovative configuration to assess gas-surface interaction during aerobraking. The resulting roll torques about the central body-axis as predicted in rarefied flow simulations were nearly twice that predicted for free molecular flow, although differences became less distinct for thermal accommodation coefficients well below unity. In general, roll torques increased dramatically with reduced accommodation coefficients employed in the simulation. In the DSMC code, periodic free-molecule boundary conditions and a coarse computational grid and body resolution served to minimize the simulation size and cost while retaining solution validity.

NOMENCLATURE

A_f	vehicle frontal area (236.8 cells^2)
a	thermal accommodation coefficient
D	diameter of the HGA (370 cm, 11.77 cells)
F	aerodynamic force coefficient
Kn	Knudsen number, λ/D
M	mach number or moment coefficient
m	molar mass of atmospheric gas
n	number density
Q	incident free-stream energy flux, $\rho_\infty u_\infty^3/2$
q	net heat flux on solar panels
T	temperature
u	flow velocity
x-axis	roll axis, along central body axis
y-axis	yaw axis, through solar panel axes
z-axis	pitch axis
α	intermolecular potential exponent
ϵ	surface radiative emissivity
λ	gas mean free path
ρ	gas mass density (kg/m^3)
∞	free-stream value

Geometric Components:

ALTA	altimeter antenna
BUS	equipment bus
FEM	forward equipment module
HGA	high gain antenna
LGA	low gain antenna
MGA	medium gain antenna
PAN	solar panels
REM	rocket engine module
SRM	housing from solid rocket motor

INTRODUCTION

The Magellan spacecraft has been mapping the surface of Venus from a highly elliptic orbit (eccentricity, e = 0.39) since September of 1990. Mission planners at NASA's Jet Propulsion Laboratory (JPL) would like to circularize the orbit to improve mapping but cannot perform the manuever through thruster activity alone due to limited remaining propellant. The orbital maneuver will be achieved through a series of gentle passes through the Venus atmosphere (approximately 840 passes with an average velocity decrement of 1.5 m/s each)[1] which were initiated on May 27, 1993. Besides circularizing the orbit, these maneuvers will provide considerable data related to atmospheric entry of satellite spacecraft.

The spacecraft configuration is depicted in Fig. 1 in its nominal entry orientation (three-axis stabilized) with flow directed along the central body axis (x-axis) such that the high gain antenna is aft. The solar panels in this configuration are normal to the flow, but may be canted at any angle (about y-axis) to form an effective "windmill" during entry. The restoring roll torques on the spacecraft may

* Research Scientist. Member, AIAA.
Mailing Address: NASA Ames Research Center
M/S 230-2, Moffett Field, California 94035-1000
† Retired. Currently Vice President, Tactical Technical Solutions
Mailing Address: PO Box 656, Broomfield, CO 80038

be measured along with surface heating and orbit altitudes to deduce the flow-field density and the surface accommodation coefficients in the normal and tangential directions. Axes for pitch and yaw are indicated in the front view.

One critical mission constraint is the aerodynamic heating on the delicate solar panels during each aeropass. Direct particle simulations of entry at several altitudes from 125 km to 140 km in the nominal orientation[2] verified that this heating was within the specified tolerance at altitudes exceeding 135 km. At the nominal altitude of 140 km, the heating and drag results corresponding to the rarefied flow were very close to those corresponding to free molecular (collisionless) flow at that altitude.

Mission planners are also concerned with spacecraft stability during aerobraking, particularly if the entry orientation has a high angle of pitch or yaw. Simplified aerodynamic analyses rely upon the assumption of free molecular flow and may be computed reliably with the FREEMAC code.[3] However, this assumption may not be valid at nominal flight conditions when the free-stream Knudsen number is below ten (based upon the HGA diameter). The objective of the present study is to calculate torques, forces, and heating of the Magellan spacecraft for several entry attitudes employing a DSMC particle method which is not restricted to the assumption of free molecule flow. The results of the rarefied simulation may then be compared to FREEMAC results to assess the significance of molecular collisions in the flow. A similar study by Rault[4] employed a DSMC method and a very fine body resolution. Unfortunately, some of those results are questionable since they differed significantly from FREEMAC results even when simulating free molecule conditions.

Roll torques associated with the windmill entry configurations were also computed in the present work at nominal conditions and compared to free molecule results. Aerodynamic sensitivity to the assumed surface thermal accommodation coefficient was assessed for the windmill configuration. The nominal altitudes were 136–140 km and the periapsis velocity was u_∞ = 8.6 km/s.

PARTICLE SIMULATION METHOD

Direct simulation Monte Carlo (DSMC) particle methods model the motion and interaction of thousands or millions of computational particles to simulate gas dynamics.[5] Specifics of the DSMC code employed in these studies are provided in Ref. 2. Given a particular position, velocity, and internal energy status, each particle in the flow-field travels unobstructed along the linear trajectory of its velocity vector over the duration of a single time step. Neighboring particles are then identified throughout the flow-field and paired-off as potential collision candidates. The flow-field is divided into a network of uniform cubic cells to facilitate identification of neighboring particles and to define the finest resolution for sampling macroscopic flow properties. Employing probabilities as functions of individual collision parameters such as collision cross-section and relative translational speed[6], the subset of all candidate pairs which collide during the timestep are identified. In simulating free molecule flow, the probability of collision is artificially set to zero, representing an infinite molecular mean free path.

The entire simulated flow-field is initialized with free stream conditions. The particle simulation then runs through a transient phase as the solution develops and flow-field structures form. Upon reaching steady-state, the simulation collects statistical samples for measuring properties of the flow-field and body surface fluxes.

The DSMC code employed in the present study was developed by McDonald[7] for efficient implementation on vector supercomputers. This code simulates non-reactive, three-dimensional, flow of general gas mixtures about arbitrary geometries. Molecular collisions pertain to the Variable Hard Sphere model of Bird[8,6] with an inverse intermolecular potential exponent of α = 5 to simulate the gas dominated by CO_2 . The internal energy modes are modeled with three fully-excited degrees of freedom to account for molecular rotation and vibration. Internal energy excitation is performed with the mechanics of Borgnakke and Larsen[9] employing a fixed probability of relaxation of 1/5.

Body Geometry and Grid

The geometry of the Magellan spacecraft is shown in Fig. 1 and compared to the simulated geometry. Due to the large mean free path in the flow about the spacecraft, small features on the vehicle such as the altimeter antenna (ALTA), the medium and low gain antennas (MGA, LGA), and the rocket engine modules (REM) have negligible impact on the flow-field as a whole and may be excluded to simplify the simulation geometry, leading to two planes of symmetry on the vehicle. These small features do impact the vehicle aerodynamics, however, and their contribution will be considered separately.

To represent a surface in the cubic cartesian grid network of the simulation, it is necessary to approximate the surface as a composite of planar facets. Each facet has a normal defined from the intersections of the surface with the edges of the cell. This faceted description of the body is appropriate given that body radii are large in comparison to the cell size, and that the intersection of different surfaces occurs at cell boundaries. Since the solar panels and HGA are dominant components of the structure, the simulation cell network was scaled such that the square simulated panels (measuring 8 cells × 8 cells) have the same frontal area as the actual solar panels and that the HGA diameter (11.77 cells) matches the actual HGA via scaling factor, 1 cell = 31.44 cm. Such a coarse grid and body resolution was used in this study to reduce the computational expense associated with running several simulations.

Grid resolution greatly impacts the accuracy of DSMC solutions for vehicle aerodynamics and heating in rarefied flows. An established criterion for sufficient grid resolution is that the local mean free path must exceed the cell

dimension. For cold-wall blunt-body rarefied flows, flow-field density will likely be quite large near the body surface, leading to a small stagnation mean free path. Equilibrium kinetic theory provides the following estimate of the local mean free path[10] near the body surface,

$$\frac{\lambda}{\lambda_\infty} \approx \frac{n_\infty}{n} \left(\frac{T}{T_\infty}\right)^{2/\alpha} . \quad (1)$$

Simulated at nominal flight conditions, the flow density n, local mean free path λ, and temperature T along the stagnation streamline at the center of the solar panel are plotted in Figs. 2 and 3. Flow properties at the panel surface led to stagnation mean free paths in the range $1.8 < \lambda < 4.2$ cells, exceeding the minimum accuracy criterion at all altitudes.

Body surfaces are modeled[11,12] as if in radiative equilibrium with deep space at a temperature of 4 K and with an emissivity of $\epsilon = 0.82$. Advantages of this model include: 1) it is simple to implement in the simulation; 2) it does not require a prescribed estimate of surface temperature; and 3) it allows each surface facet to reach its own temperature independent of neighboring facets. It is assumed that radiation from the flow-field or from other body surfaces would contribute negligibly to the net heating of a given surface facet. Most results will employ a thermal accommodation coefficient of unity, typical of rough cool surfaces facing into the flow. Molecules reflect diffusively from the surface with translational and internal energies sampled at the surface temperature. Effects of lower accommodation coefficients will also be assessed.

Flow Boundary Conditions

In simulating highly-rarefied flows, the computational flow domain must extend far enough upstream of the body to provide ample opportunity for free-stream molecules to interact with those molecules that have reflected from the body and are diffusing into the flow. Insufficient upstream domain size leads to overprediction of aerodynamic heating and forces.[2,13]

Taking advantage of body symmetry, the simulated flow-field configuration is that of a wind tunnel depicted for pitch simulations in Fig. 4 (100 L × 84 H × 18 W in cells) with a specularly-reflecting symmetry plane and a free-molecular outer plane. Particles which strike the outer plane after reflecting off of a body surface are removed from the flow field. All other particles striking the outer plane reflect specularly back into the flow. This effectively reduces the influence that the outer wall has upon the flow near the vehicle in highly-rarefied or free molecular flows.

Particles enter the flow domain from the left plane at the specified pitch angle, and exit normally from the right plane. The top and bottom planes represent free-molecular periodic boundary conditions. Again, particles which had reflected from the body before striking these planes are removed from the simulation. All other particles striking one of these planes simply re-enter the flow domain from the opposite plane, maintaining their velocity vectors. This boundary condition still provides free-stream flow approaching the body geometry while reducing the required height of the wind tunnel, therefore minimizing the size and cost of the simulation.

SIMULATION RESULTS

Employing a free-stream flow speed of u_∞ = 8.6 km/s and the day-side atmospheric data of Keating[14], simulations were performed for several entry attitudes of pitch, yaw, and solar panel canting. Flight conditions are listed in Table 1 for each altitude. Results from the particle simulation for rarefied flows, employing the finite molecular mean free path, were compared to free molecular (collisionless) simulation results. These were, in turn, compared to analytic free molecular results generated with the FREEMAC code[3] which employs ray-tracing algorithms to assess aerodynamic coefficients of spacecraft. FREEMAC results assumed that all surfaces have a fixed temperature of 300 K. The DSMC code predicted surface temperatures near 400 K for the solar panels using the radiative equilibrium model described above.

Limited computational resources and the large number of cases investigated in the present study restricted the number of particles which could be employed in the simulation to just four particles per cell in the free-stream. However, density gradients in the flow-field significantly increased the particle densities near body surfaces such that 400,000 particles existed typically in the flow-field at steady-state. Employing roughly 6,000 transient steps and 6,000 steady-state sampling steps in the simulation, the number of statistical samples was sufficiently large to yield accurate and meaningful solutions. Run-times averaged 1.0–2.0 CPU hours per case on the Cray-YMP supercomputer with a nominal computational performance of roughly 1.1 μsec/particle/timestep. The simulation could have employed ten times as many particles but would have required a ten-fold increase in computational time per case which was not warranted in the present study.

The simulation computed the net force and heat flux upon each surface facet of the vehicle. Torques were computed by the moments of body forces about a reference point defined by the intersection of the central body axis (x-axis) and the solar panel axis (y-axis). This reference point is very close to the spacecraft center of mass. Coefficients for forces (F) and moments (M) are defined from free-stream properties u_∞ and ρ_∞, the simulated frontal area A_f, and a reference length for moments given by the HGA diameter D.

Pitch and Yaw Aerodynamics

Moment coefficients for pitch and yaw attitudes (0° – 90°) are plotted in Figs. 6 and 5 as computed with the FREEMAC and DSMC codes. The thermal accommodation coefficient was fixed at unity for both codes. For all cases, the resulting moments acted to return the vehicle to its nominal zero-pitch, zero-yaw attitude. Yaw moments

rose smoothly, reaching a peak at roughly 45° before dropping again. The pitching moment, however, had two local maxima (at 20° and 70°) and a local minimum (at 50°). This behavior resulted from the solar panels shading the HGA partially from the incident flow at those attitudes.

The DSMC method was used to simulate rarefied flows (finite mean free path) at 136 km and 140 km. Repeating these simulations under free molecular conditions yielded results which were nearly indistinguishable between the two altitudes. Note that the DSMC free molecular results agree fairly well with those from FREEMAC. Slight differences are likely due to different surface temperature models employed in each code and the fact that FREEMAC neglects multiple reflections of molecules with vehicle surfaces. More important, however, is the observation that rarefied and free molecular DSMC results do not differ dramatically, indicating that molecular collisions do not alter the vehicle aerodynamics significantly. The moments for rarefied flow at 136 km are roughly 7 – 10% below the free molecular results, except at high pitch and yaw attitudes. Results are similar at 140 km.

Other aerodynamic properties under pitch and yaw are plotted in Figs. 8 and 7. These include force coefficients in the direction of the body axis (F_x), in the perpendicular directions (F_y and F_z), and in the flow direction (drag, C_D). The net heat flux q on the windward solar panel is plotted relative to the incident free-stream energy flux, Q. For all coefficients, the effects of flow rarefaction led to small yet noticeable differences from free molecular results. These differences are greatest at lower pitch and yaw attitudes, where the solar panels and HGA led to greater wetted area of the vehicle. At attitudes near 90°, the wetted area was significantly smaller such that the flow was effectively more rarefied, leading to little distinction between rarefied and free molecular results.

Effect of Body Resolution

The FREEMAC and DSMC results above employed the same coarse body resolution. This was sufficient to demonstrate the small differences between rarefied and free molecular flow models. However, the FREEMAC code may employ a fine body resolution which more precisely resembles the actual vehicle configuration, including small features such as the MGA, LGA, ALTA, and REM. These small features would not alter the effects of flow rarefaction demonstrated above, but they do impact the magnitudes of vehicle aerodynamics. FREEMAC moment and drag coefficients for each body resolution are plotted in Figs. 9 and 10. Note that the same general pitch and yaw characteristics result for each body resolution, but that the magnitudes of each differ somewhat. Accurate estimation of the vehicle aerodynamics would therefore require adjusting the fine-resolution FREEMAC results to account for the small rarefaction effects demonstrated with the coarse-resolution above.

"Windmill" Roll Aerodynamics

A creative experiment suggested by Lyons and Hurlbut[15] for Magellan aerobraking would involve canting the solar panels in opposite directions to create a "windmill" configuration with the spacecraft. Measuring the restoring roll torques induced by the spacecraft control system would provide insight into rarefied hypersonic gas-surface interaction. This windmill configuration was simulated with the DSMC code in the present work for flow in the nominal direction (along the body-axis) at 138 km altitude. The solar panels were canted at angles of $0°, 7.2°, 22.0°, 41.4°, 60°, 75.5°$, and $90°$, where 0° is perpendicular to the incident flow. The thermal accommodation coefficient was fixed at unity. Coefficients for drag, roll moment, and panel heating are plotted in Fig. 11. Drag and heating results exhibit the same differences between rarefied and free molecular flows as predicted above from the pitch and yaw simulations. However, the roll moment coefficients M_x in the rarefied simulations were nearly twice as large as those in the free molecular flows. Although these roll moments are very small, and therefore statistically sensitive, they exhibit this behavior consistently for all cant angles.

This surprising behavior is unlike all other aerodynamic observations in this study, leading to concern about solution validity. It was suggested that perhaps the DSMC flow domain was so small that particles diffusing out of the periodic simulation boundaries were reflecting back toward the body, thus altering the roll characteristics of the vehicle. The simulations were repeated three times with consecutively larger lateral domains (in y and z directions). The distance between the vehicle surfaces and the nearest boundary were increased by factors of three, six, and twenty. Nonetheless, the roll moment coefficients for each case differed from the original by less than five percent. These results indicate that, indeed, the roll moment for the windmill configuration is small but highly sensitive to molecular collisions in the rarefied flow-field.

Effects of Surface Accommodation

In the DSMC code, a thermal accommodation coefficient of, say, a=0.8, means that particles have a 20% chance of reflecting specularly from a surface and an 80% chance of reflecting diffusely with energies sampled at the surface temperature. Windmill roll-moment calculations with panels canted at 41.4° were repeated using thermal accommodation coefficients of $a = \{0.6, 0.7, 0.8, \text{and } 0.9\}$. Results for free molecular and rarefied flows are plotted in Fig. 12. With increasing thermal accommodation coefficient, the roll moment dropped rapidly while panel heating increased. More importantly, the distinction between rarefied and free molecular results was significant only for coefficients above a=0.80. This observation further supports the assertion that the windmill experiment would provide valuable flight data regarding surface accommodation and flow-field properties under these conditions.

CONCLUDING REMARKS

The aerodynamics of the Magellan spacecraft during proposed entry into the atmosphere of Venus may be computed for free molecular flows with the FREEMAC code. However, at nominal altitudes near 140 km, where the free-stream Knudsen number drops below Kn=10, the free molecular flow assumption could be questionable. This study computed the body torques on the spacecraft, when entering with various off-design attitudes, using a DSMC particle method for rarefied flow conditions. Repeating these simulations for collisionless flow provided a direct means of assessing the significance of molecular interactions in the flow, as well as providing a means to validate the technique through comparison to FREEMAC results. At all pitch and yaw attitudes, molecular collisions tended to reduce the aerodynamic forces, moments, and heating below free molecular values by 7–10%. All body torques acted to restore the vehicle to its nominal zero-pitch, zero-yaw attitude. Canting of the solar panels yielded roll moments which were highly sensitive to the thermal accommodation coefficient for gas-surface interaction. For coefficients near unity, the predicted roll moments were notably larger for rarefied flows than for free molecular flows. In general, however, the DSMC calculations verified that the aerodynamics during Magellan aerobraking may be modeled within 10% error by assuming free molecular flow at the nominal entry altitudes.

ACKNOWLEDGEMENTS

The authors gratefully acknowledge the assistance and technical support of Dr. Daniel Lyons (JPL), and the support of NASA-Ames Research Center and Martin Marietta Astronautics Company for use of their facilities. This work is sponsored in part (for B.L.H.) by NASA grant NCC 2-582.

REFERENCES

[1] LYONS, D.T, SJOGREN, W., JOHNSON, W.T.K., SCHMITT, D. AND MCRONALD, A., "Aerobraking Magellan", *AAS Paper No.* 91-420, Durango, Colorado, Aug., 1991.

[2] HAAS, B.L. AND FEIEREISEN, W.J., "Particle Simulation of Rarefied Aeropass Maneuvers of the Magellan Spacecraft," *AIAA Paper No. 92-2923*, July 1992. Revision to appear in *Journal of Spacecraft and Rockets.*

[3] FREDO, R.M. AND KAPLAN, M.H., "Procedure for Obtaining Aerodynamic Properties of Spacecraft," *Journal of Spacecraft*, Vol.18, 1981, pp. 367–373.

[4] RAULT, D.F.G., "Aerodynamic Characteristics of Magellan Spacecraft in Venus Upper Atmosphere," *AIAA Paper No. 93-0724*, Jan. 1993.

[5] BIRD, G.A., *Molecular Gas Dynamics*, Clarendon Press, Oxford, 1976.

[6] BAGANOFF, D. AND MCDONALD, J.D., "A Collision-Selection Rule for a Particle Simulation Method Suited to Vector Computers," *Physics of Fluids A*, Vol.2, 1990, pp. 1248–1259.

[7] MCDONALD, J.D., "A Computationally Effecient Particle Simulation Method Suited To Vector Computer Architectures," Ph.D. Thesis, Stanford University, 1989.

[8] BIRD, G.A., "Monte-Carlo Simulation In An Engineering Context," *Rarefied Gas Dynamics*, at 12th International Symposium on Rarefied Gas Dynamics, Charlottesville, VA, July, 1980.

[9] BORGNAKKE, C. AND LARSEN, P.S., "Statistical Collision Model for Monte Carlo Simulation of Polyatomic Gas Mixture," *Journal of Computational Physics*, Vol.18, 1975, pp. 405.

[10] BIRD, G.A., "Definition of mean free path for real gases," *Physics of Fluids*, Vol.26, 1983, pp. 3222–3223.

[11] HAAS, B.L., "Particle Simulation of Satellite Aerobraking with Coupled Surface Heat Transfer," presented at the *18th International Symposium on Rarefied Gas Dynamics*, Vancouver, B.C., July, 1992. To appear in published proceedings.

[12] HAAS, B.L., "Models for Dynamic Surface Temperatures During Rarefied Aeropass Maneuvers," *AIAA Paper No. 93-2765*, July 1993.

[13] HAAS, B.L., "Flow Resolution and Domain of Influence in Rarefied Hypersonic Blunt-Body Flows," *AIAA Paper No. 93-2806*, July 1993.

[14] KLIORE, A.J., MOROZ, V.I. AND KEATING, G.M., *Venus International Reference Atmosphere*, Vol. 5, No.11, 1986, pp. 142–148.

[15] LYONS, D.T. AND HURLBUT, F.C., "Measuring the Lift Coefficient in Free Molecular Flow while Aerobraking Magellan," presented at the *18th International Symposium on Rarefied Gas Dynamics*, Vancouver, B.C., July, 1992. To appear in published proceedings.

TABLE 1: Simulation Flowfield Specifications

Altitude (km)	ρ_∞ (kg/m^3)	T_∞ (K)	m (g/mole)	M_∞	Kn_∞ [(a)]
136	1.39×10^{-8}	217	40.1	35.2	2.819
138	9.24×10^{-9}	222	39.4	34.6	4.222
140	6.13×10^{-9}	225	38.9	34.0	6.324

[(a)] Based on HGA diameter of 370 cm, $\mathrm{Kn}_\infty = \lambda_\infty / D$.

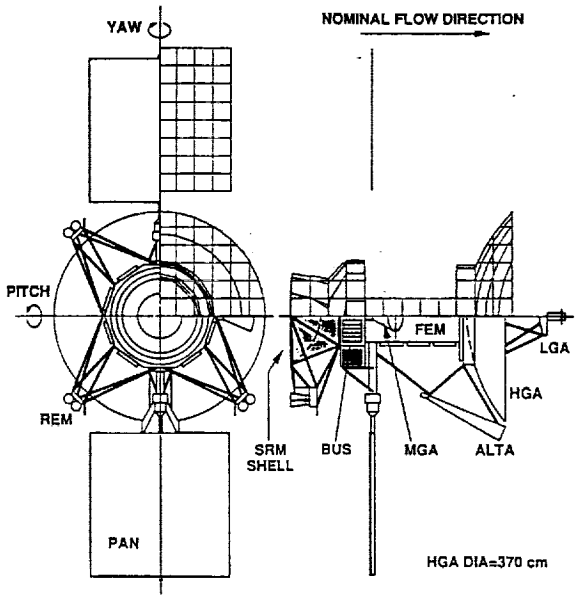

Fig. 1 Magellan spacecraft configuration versus simulated geometry shown at nominal attitude (zero pitch and yaw).

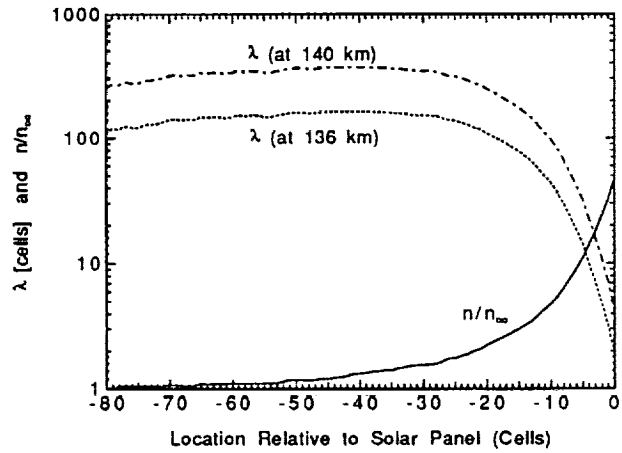

Fig. 2 Profiles of number density and molecular mean free path along the stagnation streamline ahead of the solar panel at its center (nominal attitude and flight conditions).

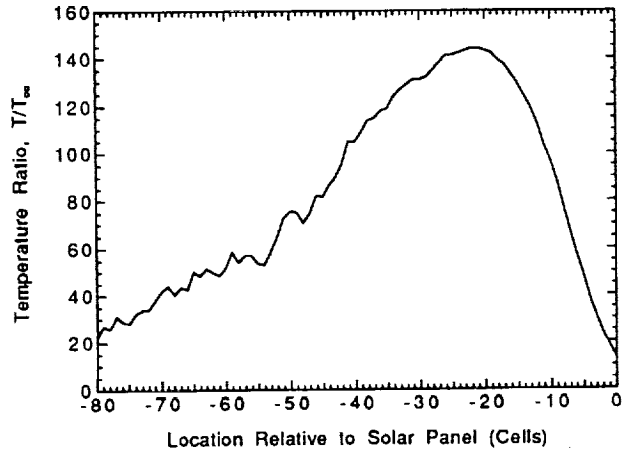

Fig. 3 Translational temperature profile along the stagnation streamline ahead of the solar panel at its center (nominal attitude and flight conditions).

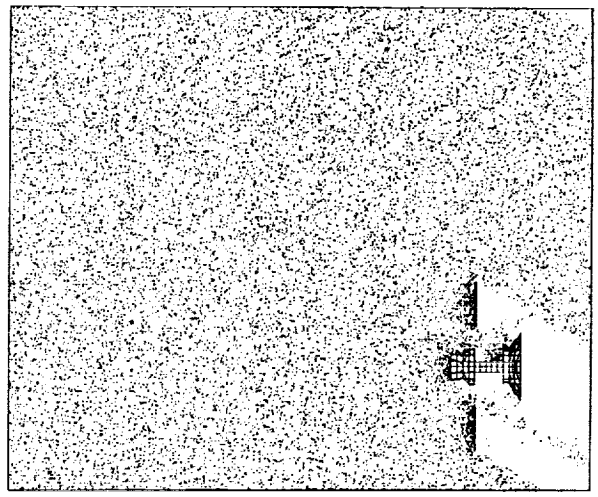

Fig. 4 Simulation geometry and flow domain for 30° pitch study. Wind-tunnel measures 100 cells in length, up to 120 cells in heigth (for 45° study), and 12 cells in width (from the symmetry plane).

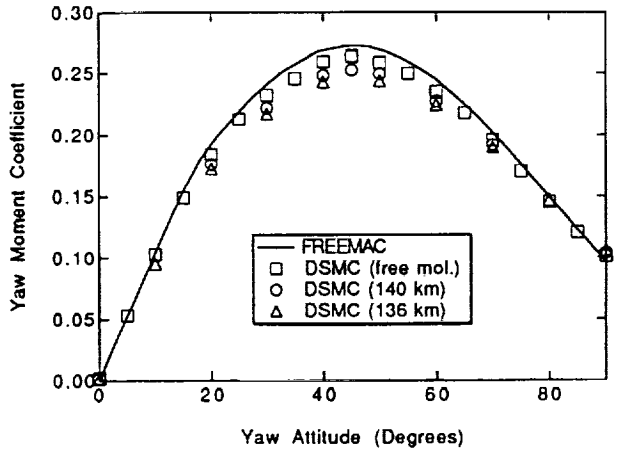

Fig. 5 Coefficient of restoring yaw moment versus entry yaw attitude. Comparison of rarefied DSMC results (at 136 km and 140 km) and free molecular DSMC and FREEMAC results.

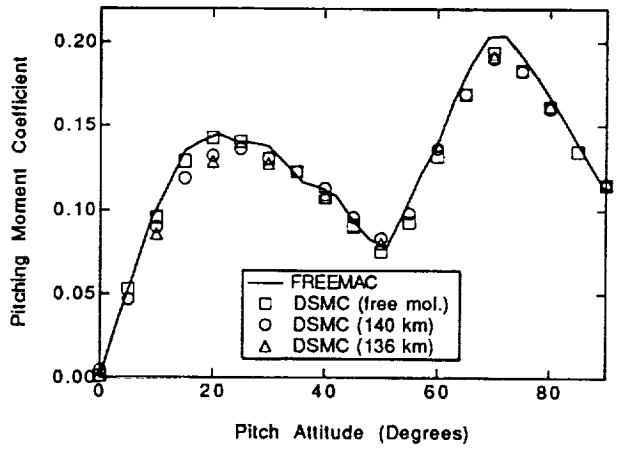

Fig. 6 Coefficient of restoring pitching moment versus entry pitch attitude.

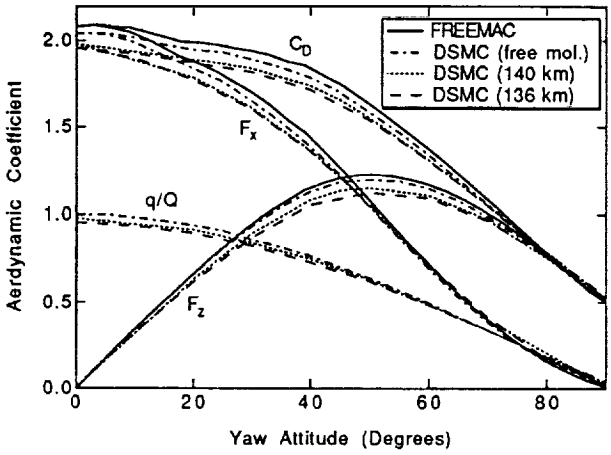

Fig. 7 Aerodynamic coefficients versus yaw attitude for drag (C_D), solar panel heating (q/Q), and forces along body axis (F_x) and perpendicular axis (F_z).

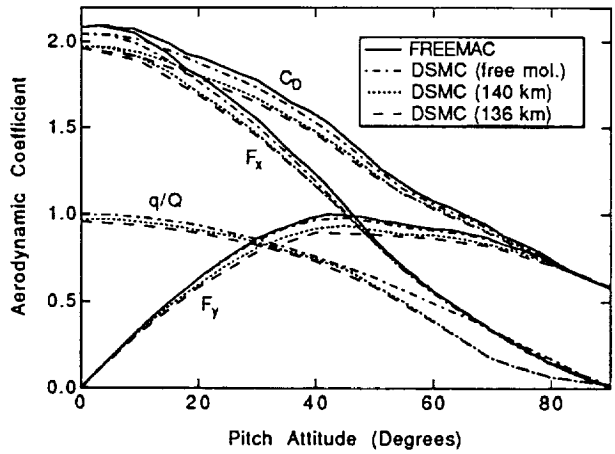

Fig. 8 Aerodynamic coefficients versus pitch attitude for drag (C_D), solar panel heating (q/Q), and forces along body axis (F_x) and along panel axis (F_y).

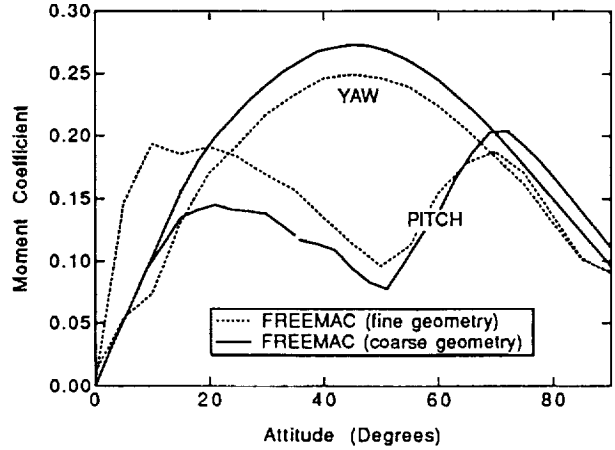

Fig. 9 Coefficients for restoring moments versus entry attitudes in pitch and yaw. Comparison of results predicted from FREEMAC code using coarse and fine body resolutions.

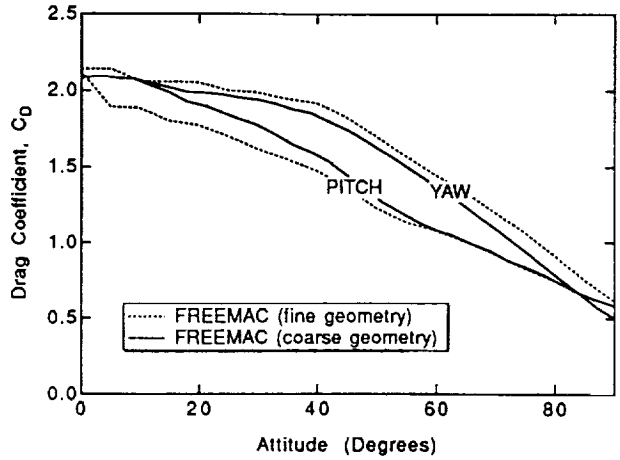

Fig. 10 Coefficients for drag versus pitch and yaw attitudes predicted from FREEMAC code using coarse and fine body resolutions.

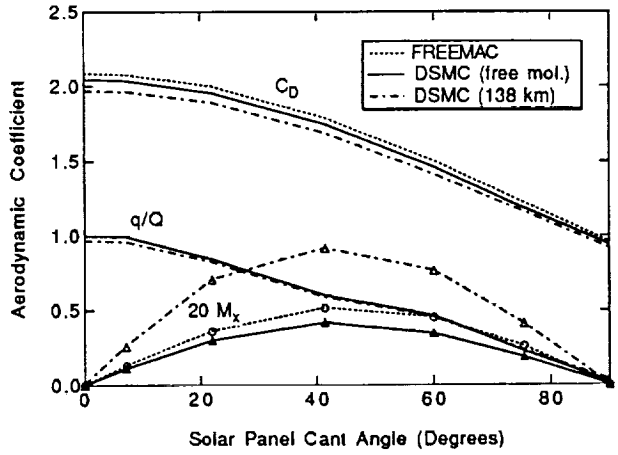

Fig. 11 Coefficients for drag, solar panel heating (q/Q), and torque (M_x, multiplied by 20) versus solar panel cant angle. Comparison of rarefied results at 138 km to free molecular predictions. Surface accommodation fixed at $a = 1.0$.

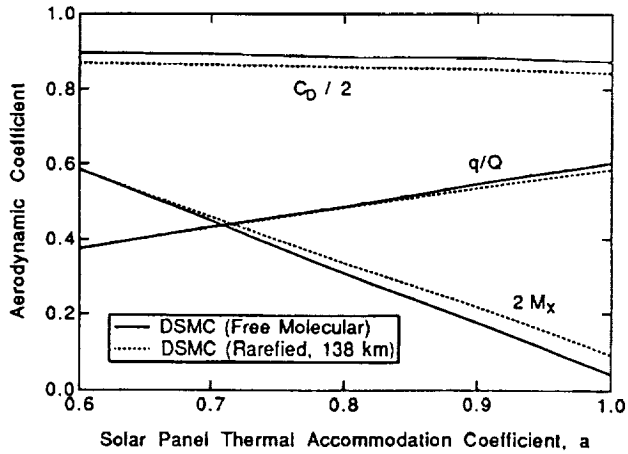

Fig. 12 Aerodynamic coefficients versus thermal accommodation coefficient a for solar panels canted at 41.4°. Comparison of rarefied results at 138 km to free molecular predictions.